이학박사 학위논문

Imaging mRNA in live neurons and animals

살아있는 뉴런과 동물에서 mRNA 관찰에 대한 연구

2021 년 8 월

서울대학교 대학원

물리천문학부

이병훈

Ph.D Dissertation

Imaging mRNA in live neurons and animals

Byung Hun Lee

Supervised by

Professor Hye Yoon Park

August 2021

Department of Physics and Astronomy

Graduate School

Seoul National University

Imaging mRNA in live neurons and animals
살아있는 뉴런과 동물에서 mRNA 관찰에 대한 연구

지도교수 박 혜 윤

이 논문을 이학박사 학위논문으로 제출함
2021 년 6 월

서울대학교 대학원
물리천문학부
이 병 훈

이병훈의 이학박사 학위논문을 인준함
2021 년 8 월

위 원 장	홍 성 철
부위원장	박 혜 윤
위 원	백 용 주
위 원	조 정 효
위 원	김 진 현

Abstract

Byung Hun Lee

Department of Physics and Astronomy

Seoul National University

mRNA is the first product of the gene expression and facilitates the protein synthesis. Especially in neurons, some RNAs are transcribed in response to stimuli and transported to the specific region, altering local proteome for neurons to function normally. Recent advances of mRNA labeling techniques allowed us to observe the single mRNAs in live cells. In this thesis, we applied RNA imaging technique not only to identify the neuronal ensemble that activated during memory formation and retrieval, but also to traffic mRNAs transported to the axon.

In the first part of the thesis, we observed the transcription site of Arc gene, one of the immediate-early gene, which is rapidly transcribed upon the neural stimuli. Because of the characteristic of expressing in response to stimuli, Arc is widely used as a marker for memory trace cells thought to store memories. However, little is known about the ensemble dynamics of these cells because it has been challenging to observe them repeatedly over long periods of time *in vivo*. To overcome this limitation, we present a genetically-encoded RNA indicator (GERI)

technique for intravital chronic imaging of endogenous *Arc* mRNA. We used our GERI to identify *Arc*-positive neurons in real time without the time lag associated with reporter protein expression in conventional approaches. We found that *Arc*-positive neuronal populations rapidly turned over within two days in CA1, whereas ~4% of neurons in the retrosplenial cortex consistently expressed *Arc* upon contextual fear conditioning and repeated memory retrievals. Dual imaging of GERI and calcium indicator in CA1 of mice navigating a virtual reality environment revealed that only the overlapping population of neurons expressing *Arc* during encoding and retrieval exhibited relatively high calcium activity in a context-specific manner. This *in vivo* RNA imaging approach has potential to unravel the dynamics of engram cells underlying various learning and memory processes.

In the second part of this thesis, we imaged β-actin mRNAs, which can generate a cytoskeletal protein, β-actin, through translation. Local protein synthesis has a critical role in axonal guidance and regeneration. Yet it is not clearly understood how the mRNA localization is regulated in axons. To address these questions, we investigated mRNA motion in live axons using a transgenic mouse that expresses fluorescently labeled endogenous β-actin mRNA. By culturing hippocampal neurons in a microfluidic device that allows separation of axons from dendrites, we performed single particle tracking of β-actin mRNA selectively in axons. Although axonal mRNAs need to travel a long distance, we observed that most

axonal mRNAs show much less directed motion than dendritic mRNAs. We found that β-actin mRNAs frequently localize at the neck of filopodia which can grow as axon collateral branches and at varicosities where synapses typically occur. Since both filopodia and varicosities are known as actin-rich areas, we investigated the dynamics of actin filaments and β-actin mRNAs simultaneously by using high-speed dual-color imaging. We found that axonal mRNAs colocalize with actin filaments and show sub-diffusive motion within the actin-rich regions. The novel findings on the dynamics of β-actin mRNA will shed important light on the biophysical mechanisms of mRNA transport and localization in axons.

Keyword: Arc mRNA, transcription, two-photon microscopy, virtual reality, neural activity imaging, memory formation, β-actin mRNA, axonal mRNA, microfluidic device

Student number: 2015-20344

Table of Contents

List of Figures

1. Introduction

1.1 Neuronal ensemble

Memory is thought to be encoded in neuronal populations called memory trace or engram cells [*1*]. The term 'engram' was first introduced by Richard Semon in the 20th century [*2, 3*]. Semon referred the engram cells to as the neuronal population that undergo persistent chemical/physical changes under an experience. A few years later, the search for engram cells were performed by Karl Lashley [*4*]. He hypothesized the engram cells are localized somewhere in the cortex. However, his study found the amount of removed cortex correlated with memory impairment, which failed to find the engram cells.

On the other hand, Donald O. Hebb, a student of Karl Lashley, proposed a theory that the neuronal population connected with each other was simultaneously activated during an experience, which often summarized as the phrase, "neurons that fire together, wire together." The cell assembly activated together strengthen the connections through synaptic changes such as long-term potentiation [*5*]. Hebb hypothesized the activation of the fraction of the cell assembly induced the reactivation of entire population. However, the efforts to understand the relation between the synaptic connectivity of cell assembly and a specific behavior memory in cell ensemble level was hindered by experimental technologies.

With recent development of technologies that activating or ablating subset of neurons, two initiative studies demonstrated that a specific memory was supported by the putative engram cells [*6, 7*]. The one study showed the ablation of the subset of neurons that highly expressing Ca^{++}/cyclic AMP-responsive element-binding protein (CREB) impaired the fear memory (Fig.

1.1A) [6]. This result is the first loss-of-function memory study at the neuronal ensemble level and suggest the neurons that express CREB during experience are allocated into engram cells. The other study demonstrated the activation of subset of neurons can mimic the memory retrieval using activity-tagging gene expression approach (Fig. 1.1B) [7]. Using tetracycline inducible gene expression approach, the dentate gyrus (DG) neuronal ensemble activated during the contextual fear conditioning (CFC) were tagged with Channelrhodopsin-2 (ChR2). The ChR2 enable neurons to activate under blue lights. The authors exposed the mice in a chamber different from the CFC chamber and photo-stimulated the neurons that activated during CFC. The photo-stimulation induced the freezing behavior which mimicked the memory retrieval process.

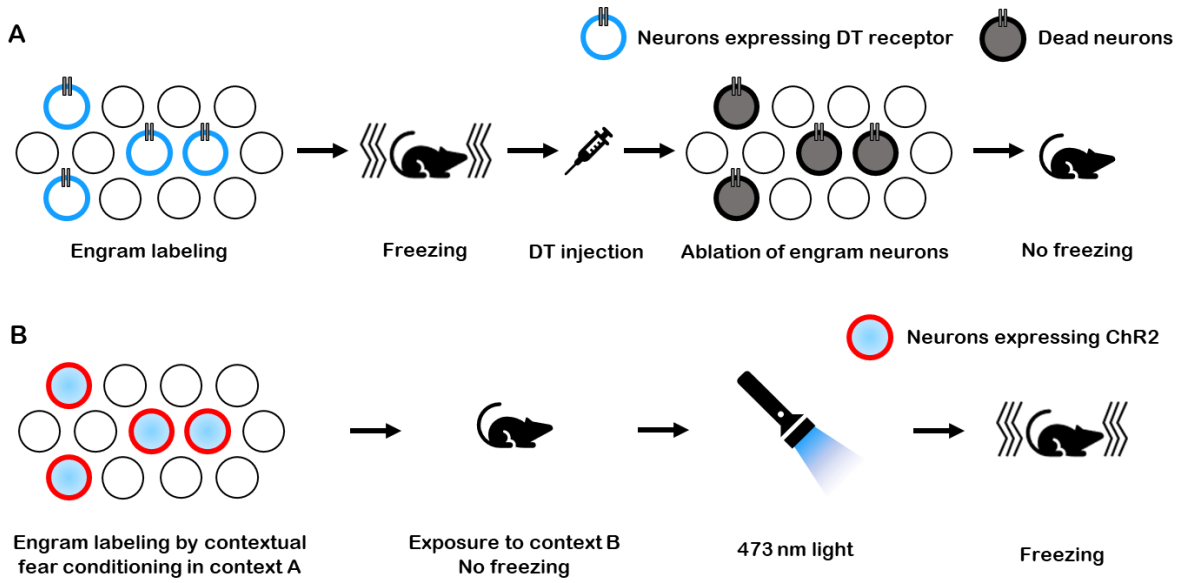

Fig. 1.1 Ablation/Activation of neuronal ensemble induced fear memory impairment/recall. (A) Overexpression of the transcription factor CREB in a certain population of neurons induced the engram allocated to the ensemble of neurons. These neurons expressed diphtheria toxin (DT) receptors which make cells die after injection of DT. Before the ablation the fear memory was intact, but after the ablation of engram cells the fear memory impaired. **(B)** Using c-Fos promotor the engram cells were labeled with channel-rhodopsin (ChR2) which make the cells activate under blue light stimulation. As the fear memory was made in context A, the mice didn't freeze in context B. Whenever the blue light was illuminated

to the engram cells, the mice showed freezing behavior which indicates the fear memory was recalled. Images adapted from [*6*] and [*7*].

1.2 Immediate-early Gene (IEG) and Arc

One of the prevalent methods to tagging neuronal ensemble that activated during an experience is using immediate-early gene (IEG) promotors [*8*]. IEGs such as *Arc* (activity-regulated cytoskeleton-associated protein), *c-Fos*, *EGR-1* (Early growth response protein 1), or *Zif268* (zinc finger protein 225) are transcribed rapidly upon cellular stimuli and used as a marker of active neurons [*9, 10*]. Using optogenetic and chemogenetic approaches, recent studies demonstrated that IEG-positive neurons are involved in putative engram or memory trace neurons [*1, 11*].

Here, our research particularly interested in the Arc gene. Arc gene has three interesting features. First, as one of the IEG, Arc gene is transcribed about 10 minutes after the stimulation and the transcripts of Arc is known to be transported to activated synapse [*12*]. Second, the Arc protein has a role in the endocytosis of AMPA (α-amino-3-hydroxy-5-methyl-4-isoxazolepropionic acid) receptors [*13*]. Due to this role, Arc is thought to be involved in long-term depression (LTD) [*14*]. Moreover, because Arc is involved in changing synaptic strength, it is not surprising that Arc knockout mouse impaired in formation of long-term memory [*15*].

1.3 Methods for identifying IEG-positive neurons

To identify the IEG-positive neurons, three methods are currently used. The one is single-molecule fluorescence hybridization (smFISH) [*9*]. This method fluorescently labels IEG transcripts using short DNA probes. The DNA probes linked with fluorescence dye target multiple RNA sequences, allowing visualization and quantification of cytoplasmic and nuclear RNAs. Using the characteristic that mRNA is transported to the cytoplasm after about 30 minutes, this method can identify the IEG-positive neurons at 30 minutes intervals. However,

not only the longer time intervals cannot be mapped, but also repeated mapping is not possible.

Another way to identifying IEG-positive neurons is fluorescence protein expression driven by IEG promotor (Fig. 1.2D) [*16-21*]. For example, Tonegawa and colleague generated a transgenic mouse [*19*], in which a coding part of Arc gene was replaced with a destabilized form of GFP (d2EGFP). The visual stimulation induced d2EGFP signal which reached a peak after 2 hours and decayed after 12 hours. However, this kind of approach has a limitation in time that the GFP signal have to be disappeared for the next stimulation.

The other way is temporally limited expression of IEG promotor dependent reporter proteins [*7, 22-25*]. The temporally limited expression techniques include tetracycline (Fig. 1.2A) or tamoxifen dependent inducible system (Fig. 1.2B-C). For example, Mayford and colleague first demonstrated the genetic tagging of c-fos active neurons [*25*]. They generated a transgenic mouse which has two transgenes, tetracycline-transactivator (tTA) with c-fos promotor and LacZ protein with tetO promotor. Because the doxycycline blocks the activation of tetO promotor, LacZ could not be expressed. The time window for labeling neurons is opened by feeding mice food without doxycycline and tTA expression activated by c-fos promotor induce the transcription of LacZ. However, the tagging window time lasts from hours to days, concerns about over-tagging have been discussed [*11, 21*].

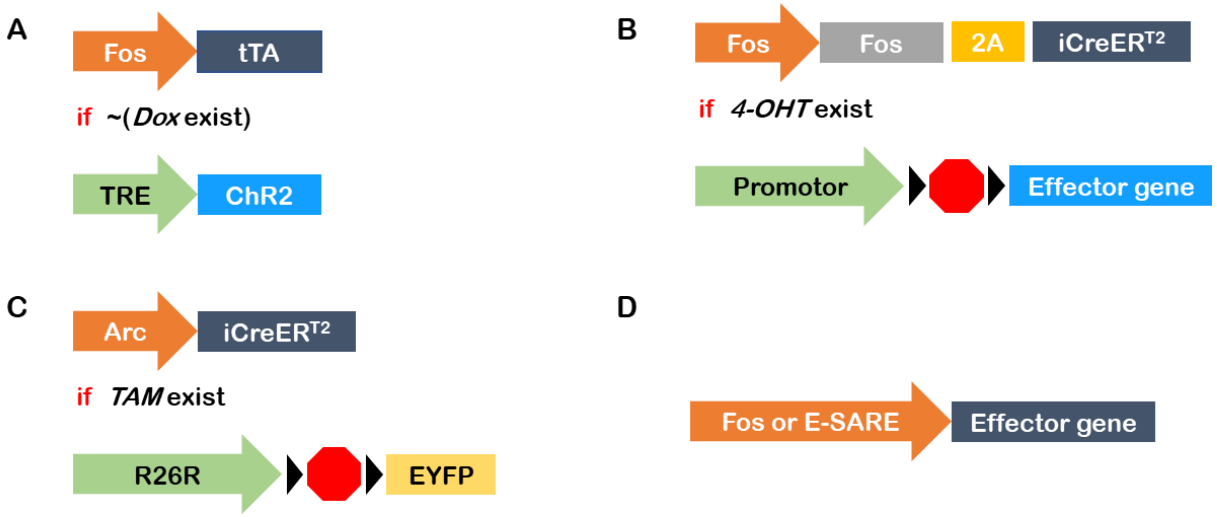

Fig 1.2. Methods to label IEG-positive neurons. (A) Fos promotor is activated under neural activity and express tTA. With the absence of doxycycline (dox), channel rhodopsin is expressed by Tet response element (TRE) promotor. This system is used in [*7*]. **(B)** Under Fos promotor, iCreER^{T2} is expressed. The 4-hydroxytamoxifen (4-OHT) induces Cre-lox recombination which induces the expression of effector gene. This system is used in [*22*]. **(C)** Using Arc promotor, iCreER^{T2} is expressed upon neural activity. The Cre-lox recombination induced by tamoxifen (TAM) makes EYFP express. This system is used in [*23*]. **(D)** The effector gene expression is driven by Fos or synaptic activity-responsive element (SARE) promotor. This system is used in [*19, 21, 26*].

To overcome these limitations, our research employed a new approach that imaging the Arc mRNA directly. To visualize the Arc mRNA, we used a transgenic knockin mouse, referred to as PCP×PBS mouse, in which all neuronal Arc mRNA is fluorescently labeled. Not only the 24× PP7 binding sequence (PBS) was inserted at the 3' untranslated region (UTR) of Arc gene, but also GFP linked PP7 coated protein (PCP-GFP) is expressed in the nucleus of the neurons. When the Arc gene is transcribed, the PBS region make the 24× hairpin loops which have a high affinity with PCPs. Therefore, the single Arc mRNA can be labeled with up to 48 GFPs.

1.4 Two-photon excitation microscopy

The fluorescence materials absorb light and transit electrons in the ground state to excited state. The electrons in the excited states decay to the lowest vibrational level of excited stated and eventually return to the ground state and emit fluorescence. A conventional fluorescence microscopy excites fluorophores with shorter wavelength light and detect the emitted light of longer wavelength. However, the Rayleigh scattering which is proportional to $1/\lambda^4$ hinders fluorescence imaging especially in tissues or live brain.

To overcome the limit, two-photon excitation microscopy excites the electron with twice longer wavelength which has a benefit for imaging in tissues with less scattering. Two-photon excitation is facilitated through the virtual state which exists only for a very short time (~fs)

according to the uncertainty principle (Fig. 1.3B). Therefore, a dense package of photon generated by femtosecond pulsed laser is required. Moreover, the axial resolution of point spread function of two-photon microscopy is better than for single-photon excitation, the two-photon excitation microscopy allows the fluorescence imaging in tissues.

With the cranial window surgery which enable optical access of the live brain as described in (Fig. 1.3A) [*27*], two-photon microscopy allows to visualize single neuron in live brains. In this research, we performed the cranial window surgery which replace the mice skull with transparent coverslip and visualized the mRNA transcription sites in live mice. To our knowledge, this is the first time to visualize the mRNA transcription sites as a locus in the brain of live animals. Furthermore, to investigate the relation between the gene expression and the neural activity, we combined mRNA imaging with calcium imaging which can trace the neural activity of neurons.

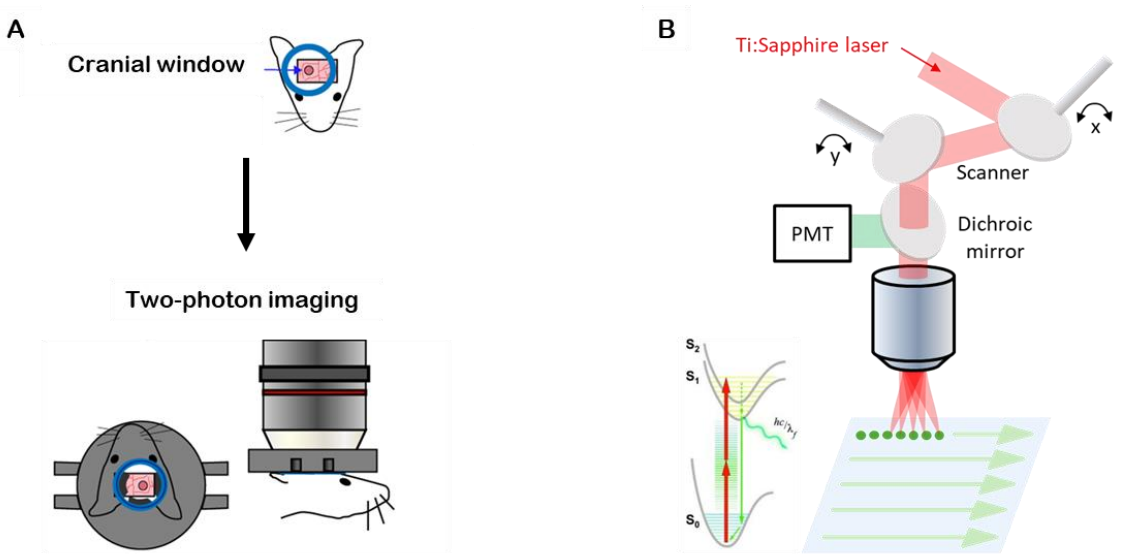

Fig. 1.3 Two-photon excitation microscopy. (A) For two-photon imaging in the live animal brain, the cranial window surgery is required. The small part of skull of the animal was drilled and replaced with transparent glass. When imaging under the microscope, the animal is fixed with customized mounting units. **(B)** Two-photon imaging is performed with a femto-second

pulsed laser, Ti:Sapphire laser, by scanning with two mirrors. Using a long wavelength laser, the electron was excited twice and decay with fluorescence emission light. The photomultiplier tube (PMT) detects the emitted fluorescence signal.

1.5 References

1. S. A. Josselyn, S. Tonegawa, Memory engrams: Recalling the past and imagining the future. *Science* **367**, (2020).
2. D. L. Schacter, *Stranger behind the engram : theories of memory and the psychology of science*. (L. Erlbaum Associates, Hillsdale, N.J., 1982), pp. 294 p.
3. R. W. Semon, L. Simon, *The mneme*. (G. Allen & Unwin ltd.; The Macmillan company, London, New York,, 1921), pp. 304 p.
4. K. S. Lashley, Mass Action in Cerebral Function. *Science* **73**, 245-254 (1931).
5. D. O. Hebb, Studies of the organization of behavior I. Behavior of the rat in a field orientation. *J Comp Psychol* **25**, 333-353 (1938).
6. J. H. Han *et al.*, Selective Erasure of a Fear Memory. *Science* **323**, 1492-1496 (2009).
7. X. Liu *et al.*, Optogenetic stimulation of a hippocampal engram activates fear memory recall. *Nature* **484**, 381-U415 (2012).
8. K. Minatohara, M. Akiyoshi, H. Okuno, Role of Immediate-Early Genes in Synaptic Plasticity and Neuronal Ensembles Underlying the Memory Trace. *Front Mol Neurosci* **8**, 78 (2016).
9. J. F. Guzowski, B. L. McNaughton, C. A. Barnes, P. F. Worley, Imaging neural activity with temporal and cellular resolution using FISH. *Current Opinion in Neurobiology* **11**, 579-584 (2001).
10. K. M. Tyssowski *et al.*, Different Neuronal Activity Patterns Induce Different Gene Expression Programs. *Neuron* **98**, 530-+ (2018).
11. S. A. Josselyn, S. Kohler, P. W. Frankland, Finding the engram. *Nat Rev Neurosci* **16**, 521-534 (2015).
12. O. Steward, C. S. Wallace, G. L. Lyford, P. F. Worley, Synaptic activation causes the mRNA for the IEG Arc to localise selectively near activated postsynaptic sites on dendrites. *Neuron* **21**, 741-751 (1998).
13. S. Chowdhury *et al.*, Arc/Arg3.1 interacts with the endocytic machinery to regulate AMPA receptor trafficking. *Neuron* **52**, 445-459 (2006).
14. M. W. Waung, B. E. Pfeiffer, E. D. Nosyreva, J. A. Ronesi, K. M. Huber, Rapid translation of Arc/Arg3.1 selectively mediates mGluR-dependent LTD through

persistent increases in AMPAR endocytosis rate. *Neuron* **59**, 84-97 (2008).

15. N. Plath *et al.*, Arc/Arg3.1 is essential for the consolidation of synaptic plasticity and memories. *Neuron* **52**, 437-444 (2006).
16. K. Ghandour *et al.*, Orchestrated ensemble activities constitute a hippocampal memory engram. *Nature Communications* **10**, 2637 (2019).
17. H. Xie *et al.*, In vivo imaging of immediate early gene expression reveals layer-specific memory traces in the mammalian brain. *P Natl Acad Sci USA* **111**, 2788-2793 (2014).
18. M. Eguchi, S. Yamaguchi, In vivo and in vitro visualization of gene expression dynamics over extensive areas of the brain. *Neuroimage* **44**, 1274-1283 (2009).
19. K. H. Wang *et al.*, In vivo two-photon imaging reveals a role of arc in enhancing orientation specificity in visual cortex. *Cell* **126**, 389-402 (2006).
20. A. L. Barth, R. C. Gerkin, K. L. Dean, Alteration of neuronal firing properties after in vivo experience in a FosGFP transgenic mouse. *J Neurosci* **24**, 6466-6475 (2004).
21. A. Attardo *et al.*, Long-Term Consolidation of Ensemble Neural Plasticity Patterns in Hippocampal Area CA1. *Cell Rep* **25**, 640-650 (2018).
22. L. A. DeNardo *et al.*, Temporal evolution of cortical ensembles promoting remote memory retrieval. *Nat Neurosci* **22**, 460-469 (2019).
23. C. A. Denny *et al.*, Hippocampal Memory Traces Are Differentially Modulated by Experience, Time, and Adult Neurogenesis. *Neuron* **83**, 189-201 (2014).
24. C. J. Guenthner, K. Miyamichi, H. H. Yang, H. C. Heller, L. Q. Luo, Permanent Genetic Access to Transiently Active Neurons via TRAP: Targeted Recombination in Active Populations. *Neuron* **78**, 773-784 (2013).
25. L. G. Reijmers, B. L. Perkins, N. Matsuo, M. Mayford, Localization of a stable neural correlate of associative memory. *Science* **317**, 1230-1233 (2007).
26. M. M. Milczarek, S. D. Vann, F. Sengpiel, Spatial Memory Engram in the Mouse Retrosplenial Cortex. *Curr Biol* **28**, 1975-1980 (2018).
27. D. A. Dombeck, C. D. Harvey, L. Tian, L. L. Looger, D. W. Tank, Functional imaging of hippocampal place cells at cellular resolution during virtual navigation. *Nat Neurosci* **13**, 1433-1440 (2010).

2. Imaging Arc mRNA transcription sites in live mice

2.1 Introduction

Though there are variety of time that immediate-early genes are expressed after the stimulation, they typically expressed in an hour. Arc mRNA transcription sites have been reported to appear in about ~10 min and decay after ~20 min after exposure to a novel environment [*1*]. Moreover, Arc knockout mice impaired in long-term memory and the late phase long-term potentiation [*2*]. The function of Arc protein is known as AMPA receptor endocytosis which modifies the synapse strength [*3*]. Collectively, with the importance of Arc gene on long-term memory formation, identifying the Arc-positive neural ensemble may help on understanding how the neuronal ensemble can store and retrieve the memory.

Previous reports which used Arc promotor based labeling approach provided valuable insights about Arc-positive neuronal ensemble and the memory formation [*4-6*]. On the purpose of labeling neurons that expressed Arc during CFC, a transgenic mouse line was generated from René Hen group [*5*]. As the mice contained Arc-CreER and R26R-STOP-floxed-enhanced yellow fluorescent protein (EYFP), the Arc positive neurons can be labeled with EYFP following administration of tamoxifen (TAM). They labeled the Arc^{+} neurons during CFC with EYFP and immune-stained Arc protein after memory test. They found the significantly larger neurons re-expressed Arc upon exposure of memory test context. Another study expressed a destabilized fluorescence protein based on an enhanced form of the synaptic activity-responsive element (E-SARE) which is a part of Arc promotor [*4*]. They exposed the mice into the same context repeatedly and track thousands of CA1 neurons. Authors found stabilized pattern of E-

SARE activity over multiple visits to the same environment. However, those methods have limitations. The first method which is a TAM dependent expression has a labeling window of 48 hours and they could not track more than two time points. The other methods can track the neuron repeatedly, but due to the maturation/expression time of the fluorescence protein, it is difficult to separate signals from specific events. Besides, because the fluorescence protein must be decay for the next labeling, authors have to wait a few days.

Here, we newly generated PCP-GFP mice and crossed with previously reported Arc PBS mice [*7*], which resulted PCP×PBS mice. In this chapter, the demonstration PCP×PBS mouse to visualize the Arc mRNA transcription site in live CA1 neurons will be described. We observed the fraction of neurons with Arc mRNA transcription sites increased upon contextual fear conditioning. Moreover, after measuring the duration of Arc mRNA transcription sites, we compared our approach with a conventional method that expresses fluorescence protein driven by IEG-promotor using Monte Carlo simulation.

2.2 Materials and methods

2.2.1 Generation of PCP×PBS mouse

Animal care practices and all experimental protocols were approved by the Institutional Animal Care and Use Committee at Seoul National University. We generated a transgenic mouse line that expresses a synonymous tandem PP7 capsid protein fused with tandem GFP (stdPCP-stdGFP) [*8*] under the control of the human synapsin-1 promoter (*hSyn*). The *hSyn-stdPCP-stdGFP* transgene was flanked by two *Rosa26* arms, and the resulting DNA fragments were microinjected into zygotes from C57BL/6N wild type (WT) mice. The transgene integration site was found between positions 26,509,464 and 26,536,787 on chromosome 13 by whole genome sequencing.

Genotyping of PCP-GFP transgenic mice was performed by PCR analysis using the following

primer sets. For the PCP-GFP allele, we used forward primer hSyn_F (5′-CGACTCAGCGCTGCCTCAGTCT-3′) and reverse primer PCP_R (5′-CGTGTATCTAACCTTAGGTAGACC-3′), yielding a 383-bp product. For the WT allele, we used forward primer Ch13_F (5′-GTCTAGAGTGCTGCTTGTCTCC-3′) and reverse primer Ch13_R (5′-CTGTGCTTCAAAACCCCATGACC-3′), yielding a 733-bp product. PCR was conducted at 95 °C for 30 sec, 60 °C for 30 sec, and 72 °C for 60 sec for 35 cycles.

PCP-GFP and Arc-PBS knock-in mice were cross-bred [*7*] to obtain a double homozygous PCP×PBS hybrid mouse line. For genotyping of the Arc-PBS knock-in, we performed PCR analysis using the following primer sets. For the 5′ end, we used two forward primers, Arc PBS gt 5F (5′-TGTCCAGCCAGACATCTACT-3′) and ArcPBS gt 5R (5′-TAGCATCTGCCCTAGGATGT-3′), and one reverse primer, PBS scr R1 (5′-GTTTCTAGAGTCGACCTGCA -3′), yielding a 320-bp product for the WT *Arc* allele and a 228-bp product for the PBS knock-in allele. For the 3′ end, we used forward primer Arc PBS gt 3F (5′-GACCCATACTCATTTGGCTG-3′) and reverse primer ArcPBS gt 3R (5′-GCCGAGGATTCTAGACTTAG-3′), yielding a 332-bp product for the WT *Arc* allele and a 413-bp product for the PBS knock-in allele. PCR was conducted at 94 °C 30 sec, 55 °C 30 sec, 72 °C 30 sec for 35 cycles.

2.2.2 Western blot

Six-week-old female mice were housed in the home cage for 7 days and habituated by daily handling. On the eighth day, CFC was performed in Context A. After CFC, the mice were housed in the home cage for 1 hour and sacrificed by cervical dislocation after isoflurane anesthesia. Brain tissue extracts were prepared using T-PER tissue protein extraction reagent (Thermo Fisher Scientific, 78510) containing 1× protease inhibitor (Roche, 04693159001). 30 μg aliquots of protein were separated on 4-12% Bis-Tris polyacrylamide precast gels

(Invitrogen, NW04120BOX) in MES-SDS running buffer (Invitrogen, B0002) and transferred to nitrocellulose membranes by using the Mini Blot Module (Thermo Fisher Scientific) following the manufacturer's instructions. The following antibodies were used: Anti-Arc (1:200, Santa Cruz Biotechnology, sc-17839) and anti-GAPDH (1:100,000, Sigma, G9545) as primary antibodies, and anti-rabbit IgG conjugated to HRP (1:5,000, SA002, GenDEPOT), and anti-mouse IgG conjugated to HRP (1:5,000, SA001, GenDEPOT) as secondary antibodies. Western blots were scanned by LAS 4000 (GE Healthcare Life Sciences). The images were analyzed by Image Studio Lite Ver 5.2 (LI-COR Biosciences).

2.2.3 Single molecule fluorescence in situ hybridization (smFISH)

smFISH was performed using an RNAscope fluorescent multiplex assay (ACDBio) according to the manufacturer's protocol. After CFC, brains were harvested after decapitation and immediately frozen in -80 °C ethanol. The brains were sectioned coronally to 20 μm using a cryostat (Thermo Fisher Scientific, HM525 or Leica, CM1860) and collected on Superfrost microscope slides (Thermo Fisher Scientific, J1800AMNZ). The sections were fixed in 4% PFA at 4 °C for 15 min. Following serial dehydration in 50%, 70%, and 100% ethanol at room temperature (RT), the sections were incubated in 100% ethanol overnight at -20 °C. Sections were then treated with proteinase IV for 30 min at RT and rinsed with 0.1 M PBS. Probes were applied for 2 h at 40 °C. Sections were incubated with probes for 2 h at 40 °C and subsequently incubated with amplifiers 1–4 at 40 °C. After counterstaining with DAPI solution, the sections were cover-slipped with ProLong mounting media (Invitrogen, P36965). Images were obtained using a Zeiss slide scanner with a 20× 0.8 NA objective or a confocal microscope (Zeiss, LSM780) with a 40× 1.3 NA oil immersion objective (Zeiss, 420460-9900-000). Probes used in this study were Arc-C1 (Cat# 316911), PP7-C2 (Cat# 300031, custom-designed), c-Fos-C2 (Cat# 316921), and Egr-1-C3 (Cat# 423371).

2.2.4 Fixed brain imaging

Fixed brain slices were prepared as previously described, with minor modifications [*9*]. Mice were deeply anesthetized with isoflurane and perfused transcardially with 10-15 ml of phosphate buffered saline (PBS) containing 10 U/ml heparin (Sigma, H3393), and 30-50 ml of fresh 4% paraformaldehyde (PFA, Sigma-Aldrich, 158127) in 0.1 M phosphate buffer (PB). Brains were post-fixed in 4% PFA at 4 °C overnight, and sectioned coronally to 50 μm with a vibratome (Leica, VT1200S). The sections were counterstained with 0.1 μg/ml DAPI (Invitrogen, D1306) in PBS and cover-slipped with VectaShield mounting media (Vector Labs, H-1400). Imaging was performed using a slide scanner (Zeiss, Axio Scan.Z1) with a 20× 0.8 NA objective (Zeiss, 420650-9902-000) or a confocal microscope (Zeiss, LSM780) with a 40× 1.3 NA oil immersion objective (Zeiss, 420460-9900-000).

To image jRGECO1a in fixed brain tissues, we used a wide-field fluorescence microscope (Olympus, IX83) equipped with a 20× 0.5 NA objective (Olympus, UPLFLN20X), a motorized stage (Marzhauser), and an EMCCD camera (Andor iXon Life 888). To obtain a large field of view, we performed 15 × 18 grid imaging and stitched the images after shading correction using BaSiC software [*10*].

2.2.5 *In vivo* imaging using two-photon excitation microscopy

In vivo imaging was performed using a two-photon excitation laser scanning microscope (Olympus, FVMPE-RS) equipped with two GaAsP photomultiplier tubes (PMTs), a Ti:Sapphire laser (Mai-Tai DeepSee, Spectra-Physics), a galvo/resonant scanner, and a 25× 0.95 NA water immersion objective with an 8-mm working distance (Olympus, XLSLPLN25XSVMP2). Excitation wavelengths of 900 nm (for *Arc* transcription imaging) and 1030 nm (for jRGECO1a imaging) were used, and fluorescence was collected via

two PMTs after passing through a filter cube (Olympus, FV30-FGR) that consists of a 570 nm low-pass dichroic mirror and two emission filters (495–540 nm band-pass and 575–645 nm band-pass filters). For *Arc* transcription imaging after CFC, mice were anesthetized immediately after each behavior session by 5% isoflurane inhalation using a low-flow vaporizer (Kent Scientific, SomnoSuite) and mounted on the two-photon microscope. Anesthesia was maintained during imaging with 1~1.5% isoflurane, and body temperature was maintained at 37 °C. We scanned a volume of 250 μm × 250 μm × 20 μm at 1024 × 1024 × 81 voxels with a scan speed of 2 μs per pixel using a galvo scanner. To facilitate future relocation of regions of interest (ROIs), we marked 2~4 spots by laser ablation.

2.2.6 Cranial window surgery

For *in vivo* imaging experiments, we used 8–11-week-old male PCP×PBS hybrid mice that were heterozygous for PCP-GFP and homozygous for the Arc-PBS knock-in. Mice were anesthetized by intraperitoneal injection of ketamine/xylazine and fixed on a stereotactic frame. Chronic hippocampal windows were implanted as described previously [*11*]. Briefly, a 2.7–2.8-mm diameter craniotomy was made at AP -2.0 mm, ML +1.8 mm from the bregma by using a 2.7-mm diameter trephine drill (FST) overlying the dorsal hippocampus. The dura was removed with forceps, and the cortical tissue above the CA1 region was carefully removed by aspiration. A customized stainless-steel cylindrical cannula with a 2.5-mm Ø round glass coverslip (Marienfeld, custom order) attached at the bottom was inserted and cemented to the skull using Meta-Bond (Parkell). Chronic cranial windows over the retrosplenial cortex (RSC) were implanted at AP -1.6 mm, ML +0.5 mm from the bregma. A 2.5-mm Ø round glass coverslip, was placed on the craniotomy and sealed with Meta-Bond. Before the Meta-Bond was cured, a customized stainless-steel head ring was placed around either the cannula or the window, and fixed by adding more Meta-Bond.

2.2.7 Contextual fear conditioning

After cranial window surgery, mice were housed in the home cage for 7 days and habituated by daily handling and exposure to the anesthesia induction chamber for 5 min. On the eighth day (day 1 of the experiment), the mice were removed from the home cage and imaged under anesthesia (~1% isoflurane). On day 2, CFC was performed in Context A, which was a 250 mm × 250 mm × 250 mm acrylic box with white and black walls with yellow stripes. The chamber was equipped with a stainless-steel grid floor, an LED light, and a video camera (Canon, EOS Hi). The mice explored Context A for 180 s, and three 0.75 mA foot shocks of 2 s duration were delivered at 30 s intervals. From day 3, mice were returned to the conditioning chamber (Context A) or placed in a different context (Context B) for 180 s to assess freezing behavior induced by fear memory recall. Context B was an equilateral triangular chamber (360 mm per side) scented with 1% acetic acid. Contexts were cleaned with 70% ethanol before each session.

To assess freezing rates, we followed a method described previously [*12*], and wrote a custom MATLAB script that segments the mouse body and calculates the area of non-overlapping regions between each pair of consecutive images. If the non-overlapping area was below a threshold value for at least 0.5 seconds, the behavior was considered to be 'freezing.' The threshold value was adjusted until the freezing rate matched the manually obtained value.

2.2.8 Simulations

To compare the accuracy of the GERI and the conventional IEG-promotor based reporter expression methods for identifying the IEG-positive neurons, we generated random *Arc* activation traces for 500 neurons. At the time of stimulation, 25% of the neurons were activated during 4 min to mimic the CFC experiment. During the other time periods, each neuron has a

certain probability to activate *Arc* every minute. The Arc activation traces were then convoluted with GERI (Peak: 6 ± 1 min, half-life: 2.5 ± 1 min) or dsGFP (Peak: 120 ± 30 min, half-life: 120 ± 30 min) response functions. The peak and half-life of Arc transcription were estimated from 42 transcription sites. With several threshold, the neurons of which the intensity exceeded the threshold classified as Arc+ neurons. The simulation was repeated for 10 times to compensate the trial error. The accuracy was obtained by dividing the number of correctly predicted neurons by the number of neurons (500 neurons).

2.2.9 Electrical stimulation on cultured neurons

The electrical stimulation was applied on cultured neurons through two thin platinum wires. The cultured neurons (days in vitro 14) were infected with AAV-hSyn-jRGECO1a 3 days before the stimulation. Using isolated pulse stimulator (A-M systems, model 2100) and triggered by Arduino uno, stimulation patterns were manipulated. At intervals of 7 seconds, ten bursts were applied at 6, 8, and 10 Hz. Each burst consisted of two biphasic pulses with 2 ms duration, 10 ms interval and 3.7 V amplitude. Using wide-field fluorescence microscope (Olympus, IX83) equipped with a 20× 0.5 NA objective (Olympus, UPLFLN20X), a motorized stage (Marzhauser), and an EMCCD camera (Andor iXon Life 888), the time-lapse image of jRGECO1a was acquired at 30 frame per second (fps) during the stimulation.

2.2.10 Image analysis

For *Arc* mRNA imaging after CFC, image registration and analysis were performed with custom-written MATLAB codes (Fig. S2). Motion artifacts from breathing and cardiac function were corrected by using an auto-fluorescence image (red channel) as a reference.

Images taken on different days were aligned by rotating and translating the images. After the alignment, we subtracted the red channel image from the green channel image after normalization by maximum values to remove auto-fluorescence signals. In our PP7-GFP system, the nuclear localization sequence was added to PCP-GFP to facilitate the identification of neuronal nuclei by the GFP signal. The 3-dimensional coordinates of the cell centroids were determined by using a circle-finding algorithm in the XY and XZ plane. By examining the z-section of each cell image, two experimenters blindly classified the neurons into three groups: neurons with *Arc* transcription sites (*Arc*+), neurons without *Arc* transcription sites (*Arc*-), and not-determined (ND) cells. Neurons that showed one or two bright spots in the same XY position in at least two consecutive z-slices were classified as *Arc*+ cells. ND cells include cropped cells and cells that had PCP-GFP expression levels that were either excessive or inadequate to detect transcription sites. Any disagreement between the two experimenters was resolved by a third person.

Particles in dual-color smFISH images were detected using FISH-quant software [*13*]. FISH-quant provided sub-pixel positions and intensity by performing three-dimensional Gaussian fitting. A custom-written MATLAB script classified particles into single mRNA and transcription sites by setting thresholds for amplitude and width of three-dimensional Gaussian function (Fig. S3C). Threshold values were adjusted by examining each slice image manually. Transcription sites within 0.3 μm detected in the Atto 550 dye (CDS target) and Atto 647 dye (PBS target) channels were considered identical (Fig. S3D). To quantify the number of nascent mRNAs in a transcription site, we calculated the intensity of particles by $I = Amplitude * \sigma_x * \sigma_y * \sigma_z$ which is an integrated value of a three-dimensional Gaussian function, and divided the intensity by the median intensity of single mRNAs.

2.3 Results and discussion

To label endogenous *Arc* mRNA with GFP, we exploited the highly specific binding between the PP7 bacteriophage capsid protein (PCP) and the PP7 binding site (PBS) RNA stem-loop [*14*]. We generated a transgenic mouse that expresses a tandem PCP fused with a tandem green fluorescent protein (PCP-GFP) in neurons. The PCP-GFP mouse was crossed with the *Arc*-PBS mouse, in which 24 PBS repeats were knocked into the 3' untranslated region (UTR) of the *Arc* gene [*7*]. In the resulting PCP×PBS hybrid mouse (Fig. 2.1A) with PBS homozygosity ($Arc^{P/P}$), every endogenous *Arc* mRNA is labeled with up to 48 GFPs. Arc protein expression levels were similar in the brains of wild-type (WT), *Arc*-PBS, and PCP×PBS mice (Fig. 2.1B), indicating that PP7-GFP labeling did not disrupt *Arc* gene expression.

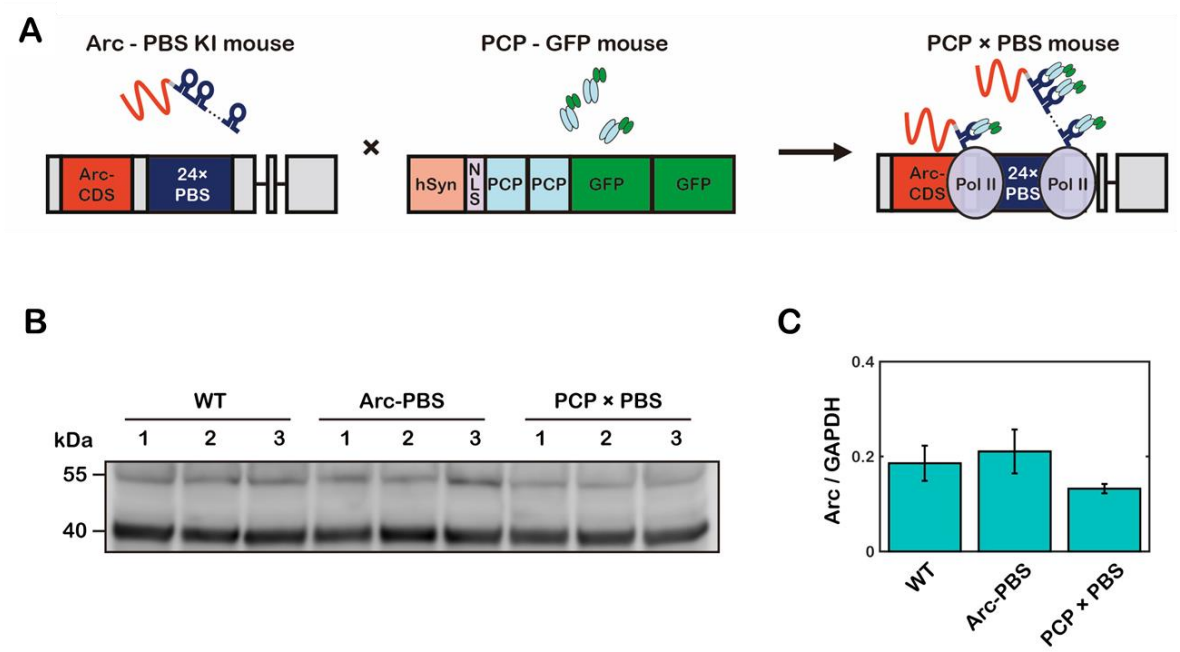

Fig. 2.1. Development of GERI mouse and comparison of Arc protein expression level of GERI and WT mouse. (A) Schematic for labeling *Arc* mRNA *in vivo*. NLS, nuclear localization sequence; Pol II, RNA polymerase II. (Gray boxes, UTR; red box, *Arc* coding sequence (*Arc*-CDS); blue box, 24× PBS cassette; black lines, introns). The *Arc*-PBS knock-

in (KI) mouse was crossed with the PCP-GFP mouse to generate PCP×PBS hybrids. **(B)** Western blot of Arc (55 kDa) and GAPDH protein (36 kDa) in brain tissue lysates of three mice from each group of wild type (WT), homozygous *Arc*-PBS knock-in (*Arc*-PBS), and double homozygous *Arc*-PBS knock-in × PCP-GFP (PCP×PBS). **(C)** Quantification of relative Arc protein expression levels using GAPDH as a loading control. No significant differences were observed between the mouse lines (n = 3 mice for each line). Error bars represent standard deviation (SD).

We first investigated the activity-dependent expression of *Arc* mRNA upon contextual fear conditioning (CFC) (Fig. 2.2A). Two-photon excitation microscopy through a hippocampal window (Fig. 2.2B) [*11*] enabled real-time monitoring of *Arc* transcription in the dorsal CA1 region (Fig. 2.2C). In a subset of neurons, one or two bright spots were clearly visible in the nucleus (red arrowheads, Fig. 2.2C).

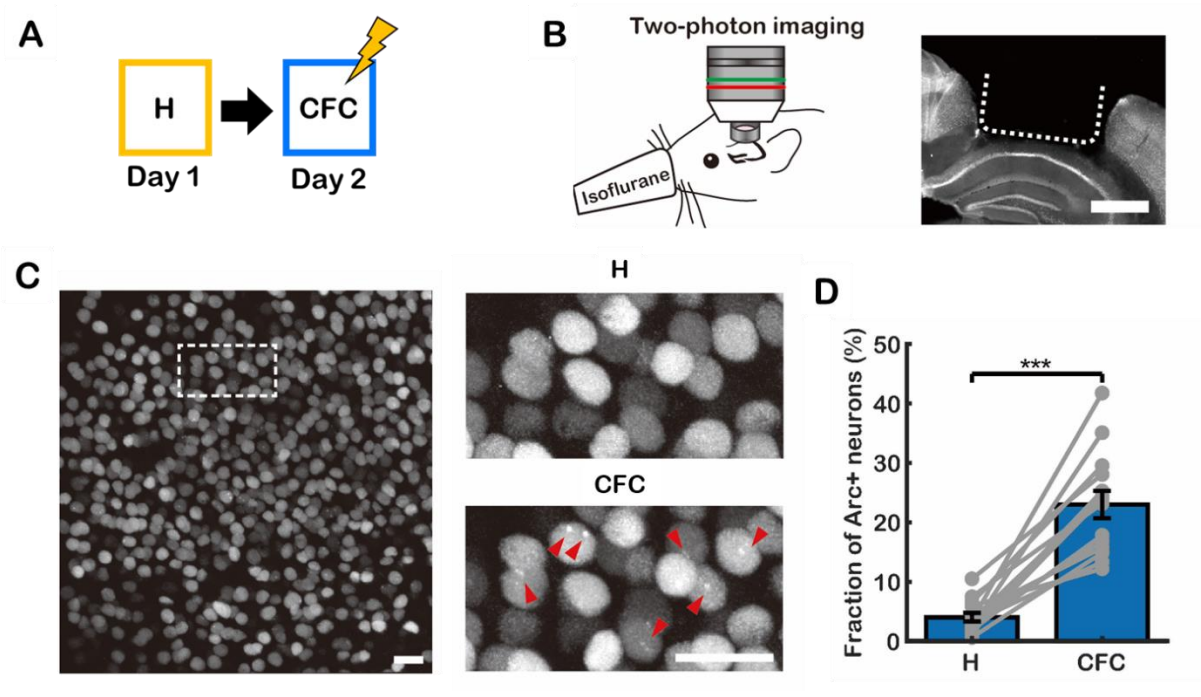

Fig. 2.2. *Arc* mRNA transcription induced upon contextual fear conditioning. (A) On day

1, mice were removed from the home cage (H) and immediately anesthetized for *in vivo* imaging. On day 2, the mice were subjected to contextual fear conditioning (CFC) followed by *in vivo* imaging. **(B)** Left, experimental set up for *in vivo* two-photon imaging through a hippocampal window. Right, coronal view of the brain of a PCP×PBS mouse after hippocampal window surgery. **(C)** Representative *in vivo* image of CA1 neurons in a PCP×PBS mouse after auto-fluorescence subtraction. The same region (dotted box) is enlarged for comparison of images taken on day 1 (H) and day 2 (CFC). **(D)** Fraction of *Arc*+ neurons in CA1 after H and CFC conditions (n = 12 mice; *** $P < 10^{-4}$ by pairwise t test). Scale bars, (B) 1 mm, and (C) 50 μm. Error bars represent SEM.

The bright point signals in the nucleus were confirmed to be *Arc* transcription sites by performing single-molecule FISH (smFISH) in brain tissues after CFC. The average copy number of nascent *Arc*-PBS mRNA per transcription site was 15 ± 4 (Fig. 2.4), which could in turn recruit ~720 GFPs to the *Arc* locus, providing sufficient signal to detect individual transcription sites located 100-400 μm deep inside the brain. For mice kept in their home cage (H), *Arc* transcription was observed in 4.1 ± 0.8% of CA1 neurons. The number of *Arc*+ neurons significantly increased to 23 ± 3% in the same regions of interest (ROIs) after CFC on the next day (Fig. 2.2D).

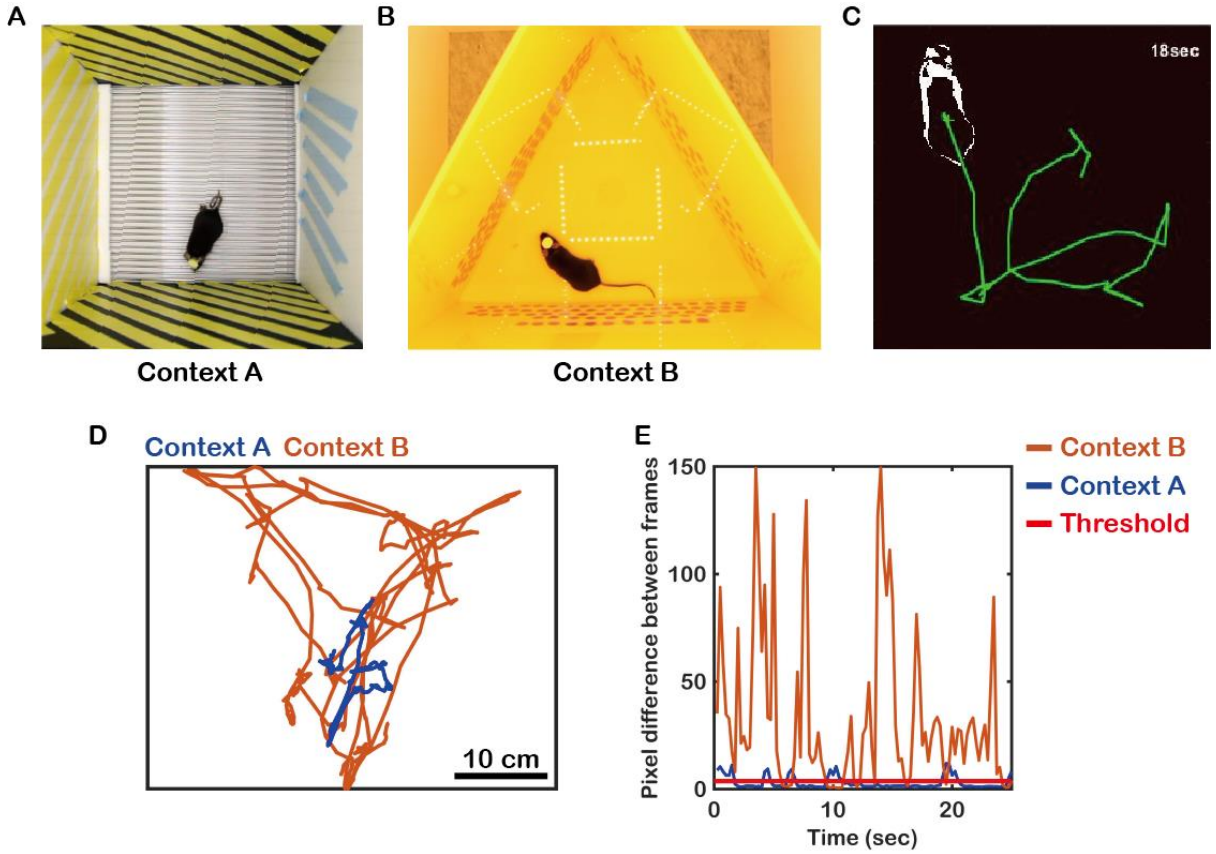

Fig. 2.3. Contextual fear memory test in context A and exposure to different chamber, context B. (A-B) The fear conditioning chamber context A (A) and neutral chamber context B (B). **(C)** The mouse centroid tracking. The pixel difference between frames are shown in white. (D) Example tracks of the same mouse in context A and context B. (E) The pixel difference between frames in context B (orange) and context A (blue) were shown.

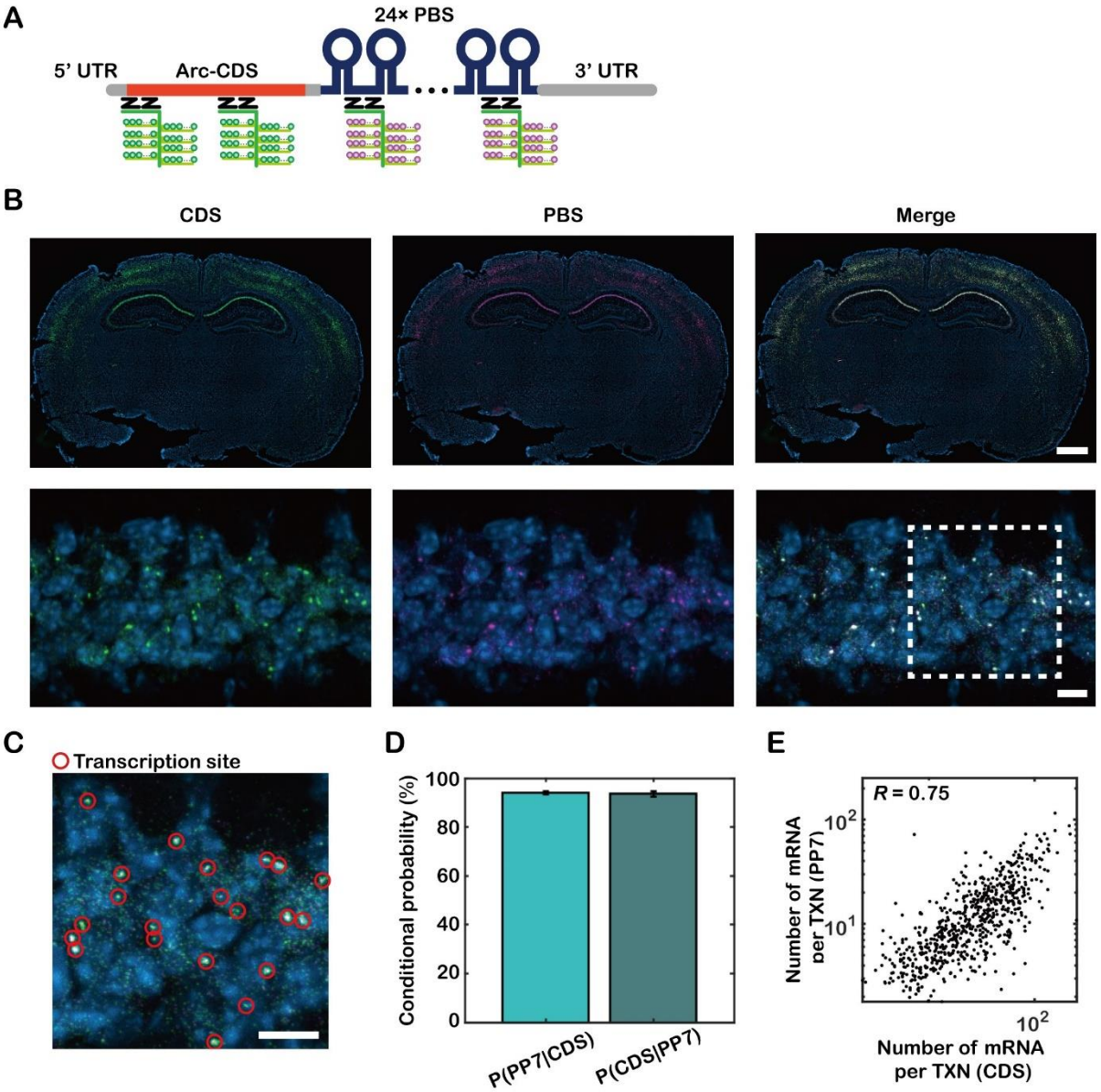

Fig. 2.4. Dual-color single-molecule fluorescence *in situ* hybridization (smFISH) targeting the CDS and PBS region of *Arc* mRNA. (A) Schematic for dual-color smFISH. The CDS region of *Arc* mRNA was detected by Atto 550 dye (green) and PBS was detected by Atto 647 dye (magenta). **(B)** Representative smFISH images. **(C)** An enlarged image of the dotted box in (B). Red circles denote transcription sites. **(D)** Conditional probability of detecting transcription sites in different channels. **(E)** Scatter plot of the number of nascent mRNAs per transcription site detected by the probes targeting CDS and PBS (n = 670 transcription sites,

correlation calculated by Spearman's coefficient *R*). Scale bars, (B, upper panels) 1 mm and (B, lower panels and C) 10 μm.

Time-lapse imaging revealed that the fraction of neurons with *Arc* transcription sites (*Arc*+ neurons) reached its maximum within 7 min and then monotonically decreased to basal levels by 20 min after CFC (Fig. 2.5A). Based on these data, a time window of 4–7 min after each behavioral test was selected for *in vivo* imaging. The time scale of Arc transcription site appearance was much shorter than that of the IEG promotor-driven fluorescence protein expression, which is a few hours. Using Monte Carlo simulations, we estimated the errors of IEG promotor-driven fluorescence protein approach and our method in identifying Arc+ neurons (Fig. 2.5). Our simulation results indicated that our method was more accurate than the previous method, especially when the basal activity exists.

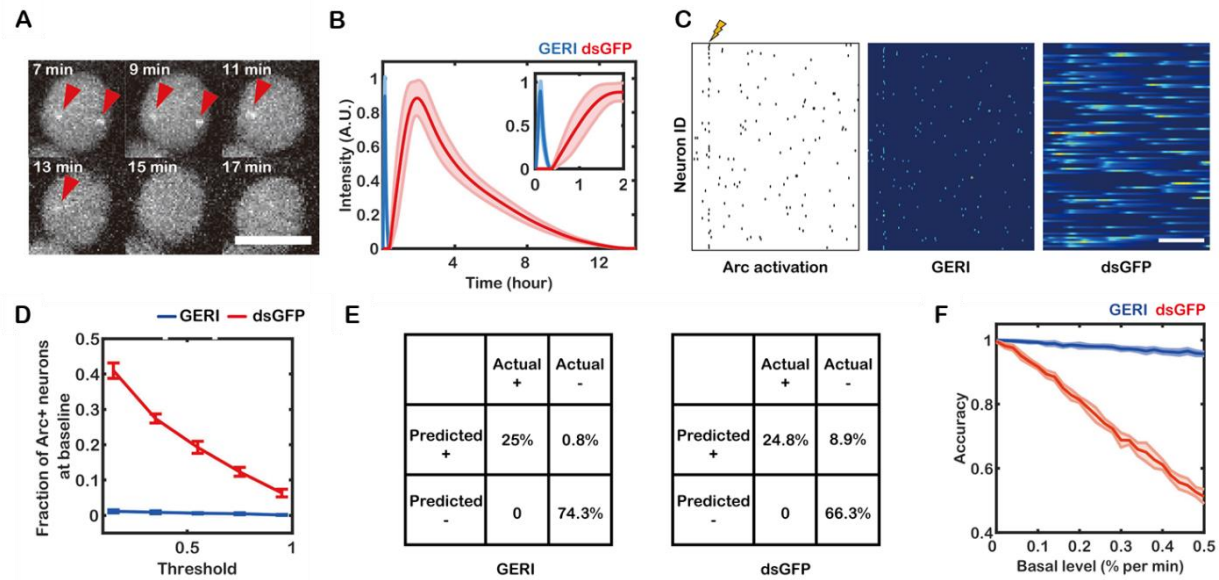

Fig. 2.5. Simulation of detection of Arc+ neurons with Arc-dsGFP or GERI approach. (A) Time-lapse images of an *Arc*+ neuron after CFC. **(B)** The intensity response functions of Arc transcription site (blue) and Arc-dsGFP (red) over time. The transcription site intensity increases after Arc activation and decays (half-life: 2.5 min) after reaching the highest point in

6 min. The dsGFP intensity reaches to the maximum after 2 hours and decays to half after 2 hours. **(C)** Example image of simulated Arc activation traces (left), and intensity traces that convoluted with the response function of GERI (middle) and dsGFP (right). In the baseline, there is a basal activity of Arc at a rate of 0.1% of neuron per minute and a stimulation induced Arc activation of 25% of neurons in 4 minutes (lightning symbol). **(D)** The fraction of Arc+ neurons at the baseline was plotted versus the intensity threshold. **(E)** In the condition (basal activity: 0.1% per min, 25% neuron activated by a stimulus), confusion matrices are represented to show how accurately each approach can predict. The intensity threshold of 0.95 and 0.15 was used for dsGFP and GERI, respectively. **(F)** The accuracy of dsGFP (red) and GERI (blue) approach was plotted at several basal levels. Error bars represent standard deviation (SD). Scale bar, (B) 6 hours.

Three-color smFISH showed that *Arc*, *c-Fos*, and *Egr-1* were regulated similarly and co-expressed in 19 ± 3% of neurons in the dorsal CA1 region after CFC (Fig. 2.6).

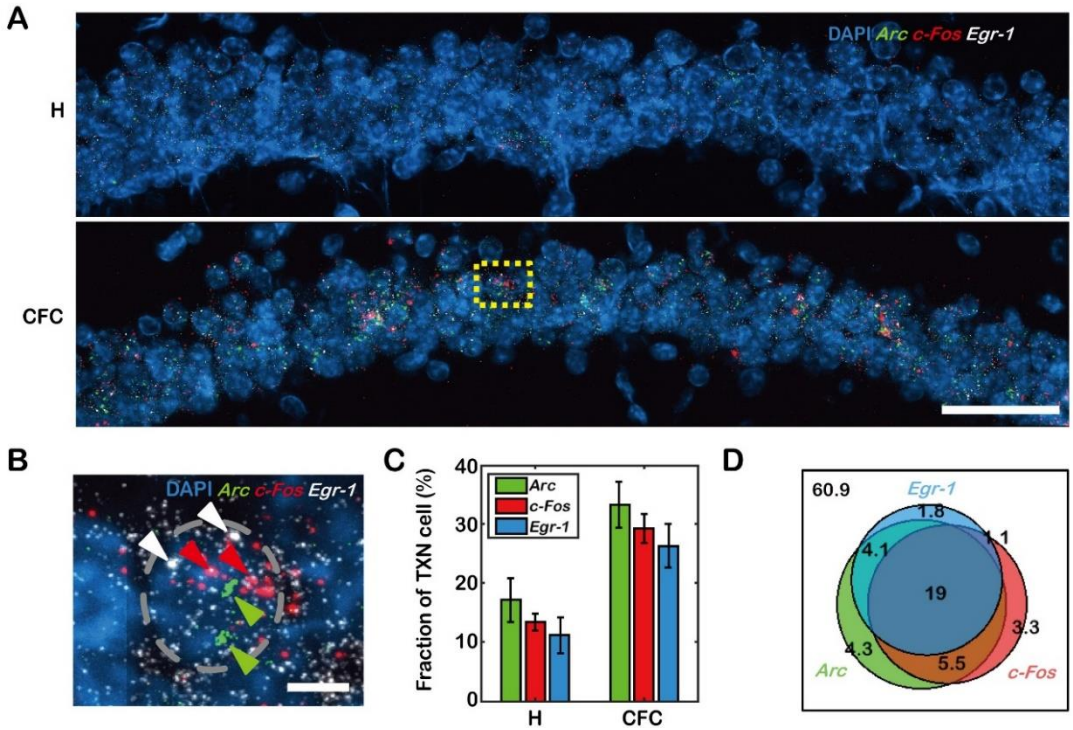

Fig. 2.6. Three-color smFISH targeting *Arc*, *c-Fos* and *Egr-1* mRNA in CA1. (A) Representative smFISH images of hippocampi from mice held in the home cage (H; upper panel) and after CFC (lower panel). *Arc*, *c-Fos* and *Egr-1* mRNA were labeled with FITC (green), Atto 550 (red), and Atto 647 (white) dyes, respectively. **(B)** Enlarged image of yellow box in (A). White, red, and green arrows indicate transcription sites of *Egr-1*, *c-Fos*, and *Arc*, respectively. **(C)** The fraction of cells with a transcription site for each gene. **(D)** A Venn diagram showing the percentage of cells expressing each gene. Scale bars, (A) 50 μm and (B) 5 μm. Error bars represent SEM.

In fixed brain sections from PCP×PBS mice, *Arc* transcription sites were readily detected by GFP signal without any staining, which facilitated RNA detection in various brain regions (Fig. 2.7).

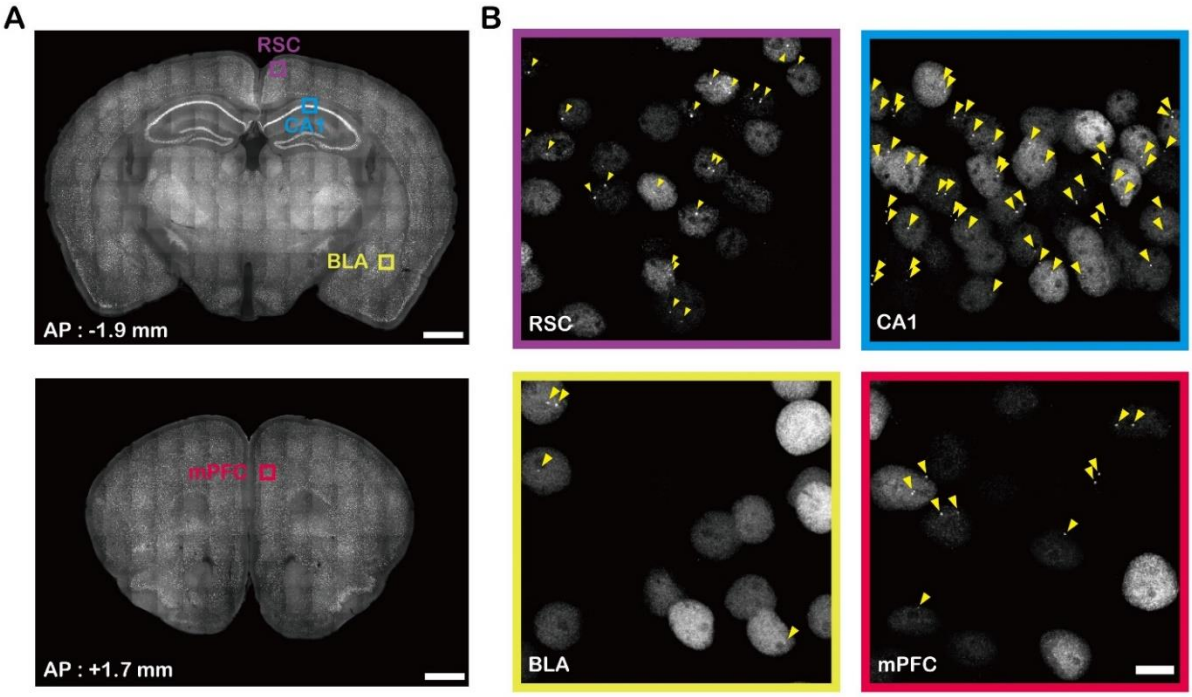

Fig. 2.7. GFP images of fixed brain slices. (A) Coronal sections of a PCP×PBS mouse brain at two AP positions (AP = -1.9 mm and +1.7 mm). Upper panel includes retrosplenial cortex (RSC), CA1, and basolateral amygdala (BLA). Lower panel includes medial prefrontal cortex (mPFC). (B) Enlarged images of the inset boxes in (A). Scale bars, (A) 1 mm and (B) 10 μm.

2.4 References

1. J. F. Guzowski *et al.*, Recent behavioral history modifies coupling between cell activity and Arc gene transcription in hippocampal CA1 neurons. *P Natl Acad Sci USA* **103**, 1077-1082 (2006).
2. N. Plath *et al.*, Arc/Arg3.1 is essential for the consolidation of synaptic plasticity and memories. *Neuron* **52**, 437-444 (2006).
3. S. Chowdhury *et al.*, Arc/Arg3.1 interacts with the endocytic machinery to regulate AMPA receptor trafficking. *Neuron* **52**, 445-459 (2006).
4. A. Attardo *et al.*, Long-Term Consolidation of Ensemble Neural Plasticity Patterns in Hippocampal Area CA1. *Cell Rep* **25**, 640-650 (2018).
5. C. A. Denny *et al.*, Hippocampal Memory Traces Are Differentially Modulated by Experience, Time, and Adult Neurogenesis. *Neuron* **83**, 189-201 (2014).
6. K. H. Wang *et al.*, In vivo two-photon imaging reveals a role of arc in enhancing orientation specificity in visual cortex. *Cell* **126**, 389-402 (2006).
7. S. Das, H. C. Moon, R. H. Singer, H. Y. Park, A transgenic mouse for imaging activity-dependent dynamics of endogenous Arc mRNA in live neurons. *Sci Adv* **4**, eaar3448 (2018).
8. B. Wu *et al.*, Synonymous modification results in high-fidelity gene expression of repetitive protein and nucleotide sequences. *Gene Dev* **29**, 876-886 (2015).
9. L. Feng, O. Kwon, B. Lee, W. C. Oh, J. Kim, Using mammalian GFP reconstitution across synaptic partners (mGRASP) to map synaptic connectivity in the mouse brain. *Nat Protoc* **9**, 2425-2437 (2014).
10. T. Y. Peng *et al.*, A BaSiC tool for background and shading correction of optical microscopy images. *Nature Communications* **8**, (2017).
11. D. A. Dombeck, C. D. Harvey, L. Tian, L. L. Looger, D. W. Tank, Functional imaging of hippocampal place cells at cellular resolution during virtual navigation. *Nat Neurosci* **13**, 1433-1440 (2010).

12. H. Shoji, K. Takao, S. Hattori, T. Miyakawa, Contextual and Cued Fear Conditioning Test Using a Video Analyzing System in Mice. *Jove-J Vis Exp*, (2014).
13. F. Mueller *et al.*, FISH-quant: automatic counting of transcripts in 3D FISH images. *Nat Methods* **10**, 277-278 (2013).
14. D. R. Larson, D. Zenklusen, B. Wu, J. A. Chao, R. H. Singer, Real-Time Observation of Transcription Initiation and Elongation on an Endogenous Yeast Gene. *Science* **332**, 475-478 (2011).

3. Neurons expressing Arc mRNA during repeated memory retrievals

3.1 Introduction

IEG-positive neurons are often referred to as engram cells, which are activated during learning and reactivated for memory retrieval [*1*]. However, the overlap between neuronal populations expressing IEGs during encoding and retrieval is relatively low, raising important questions as to whether technical limitations hinder precise identification of engram cells or if engrams have an inherently dynamic nature [*2*].

To unveil how dynamic the engram is, repeated mapping of engram neurons in the same animal. However, it has not been possible to visualize IEG-positive neurons in real time repeatedly over a long period because reporter proteins are typically expressed with a lag time longer than half an hour and a tagging time window ranging from several hours to weeks. Here, using a REGI technique, we report how the IEG-positive neuronal ensemble changes upon the same memory retrieval in recent times and remote times.

3.2 Results and discussion

3.2.1 Dynamics of Arc+ neuronal population in recent memory

Next, we investigated how the population of *Arc+* neurons changed upon CFC and repeated retrievals over three consecutive days (Fig. 3.1A). The animals showed freezing behavior during all retrieval tests (R1–3) in the conditioning context (ctx A) but not in a new context (ctx B), indicating that conditioned-context-specific fear memory remained intact (Fig. 3.1B). We performed cranial window imaging of the dorsal hippocampal CA1 region and the

retrosplenial cortex (RSC), which have essential roles in spatial cognition and memory and strong reciprocal connectivity [*3, 4*]. A similar fraction (14–20%) of neurons in CA1 transcribed *Arc* after CFC and R1–3 (Fig. 3.1C). The fraction of *Arc*+ neurons in the RSC was higher than in CA1, and increased from 24 ± 4% (CFC) to 35 ± 7% (R3) (Fig. 3.1D). Taking advantage of our live-animal imaging, we performed longitudinal analysis of *Arc* transcription history in individual neurons. We found that a distinct population of neurons expressed *Arc* mRNA every time the same contextual memory was retrieved (Fig. 3.1E). We identified the overlapping population of *Arc*+ neurons across C and R1–3 (Fig. 3.2). A small population of neurons persistently showed *Arc* transcription throughout C and R1–3 (Fig. 2E, bottom panel). This persistently overlapping population (red dots, Fig. 2F) represented 4.0 ± 0.2% of neurons in the RSC, significantly higher than that in CA1 (0.6 ± 0.1%) (Fig. 3.1G). The population of neurons that expressed *Arc* during CFC and each retrieval session also overlapped more in the RSC than in CA1 (Fig. 3.1H). Moreover, we found a positive correlation between the freezing rate and the fraction of the persistently overlapping *Arc*+ population in the RSC, whereas there was no such correlation in CA1 (Fig. 3.1I). Since the freezing rate reflects the strength of the fear memory, the persistently overlapping *Arc*+ neurons in the RSC could be a component of a stable engram for conditioned fear. Together, these results suggest that the overlapping *Arc*+ population maintains contextual fear memory in the RSC, whereas there are more dynamic changes occurring in CA1.

To assess the dynamics of *Arc* re-expression, we compared the overlap of *Arc*+ neurons with the chance level upon re-exposure to ctx A at one- or two-day intervals. In CA1, the overlap was higher than chance levels in one-day-apart groups, but became random in two-day groups (Fig. 3.1J). In the RSC, the overlap in both groups was significantly higher than by chance (Fig. 3.1K). We confirmed that the degree of overlap between *Arc*+ neurons activated during CFC

and exposure to ctx B was almost random in both CA1 and the RSC (Fig. 3.1L, M). These data indicate that there was a near complete turnover of *Arc*+ neurons responding to ctx A within two days in CA1, in line with previous reports [*5*, *6*], whereas *Arc*+ neurons in the RSC exhibited either slower dynamics or greater stability.

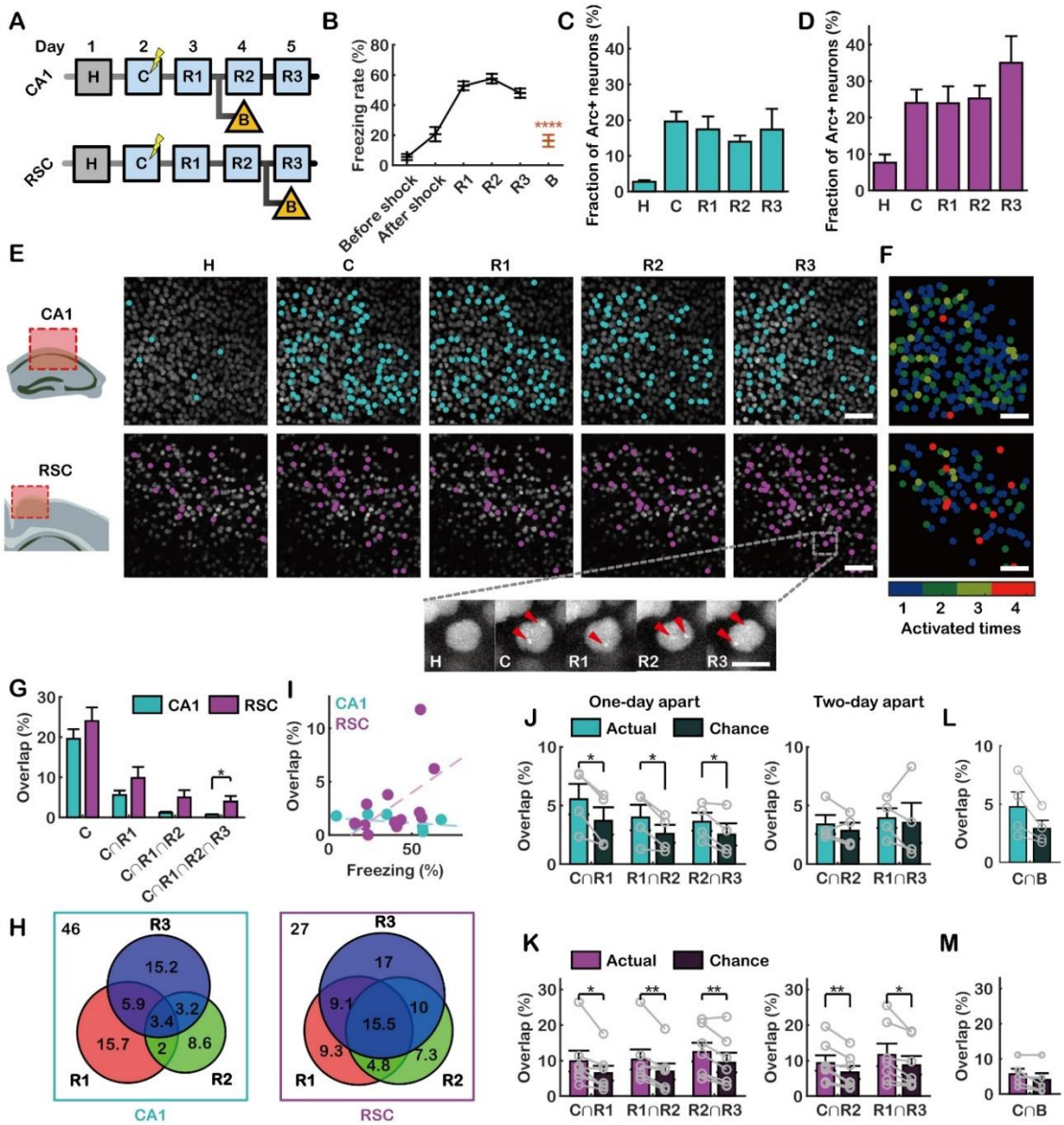

Fig. 3.1. Dynamics of *Arc*+ neuronal populations upon CFC and repeated recent memory retrievals. (A) Experimental scheme of repeated retrieval tests for three consecutive days. Groups of mice were exposed to context B on day 4 (CA1) or 5 (RSC). **(B)** Freezing rates of

PCP×PBS mice during CFC and three retrieval tests (R1–3) in context A (n = 11 mice) and context B (n = 9 mice). **(C-D)** Fraction of *Arc*+ neurons in CA1 (C) (n = 4 mice) and the RSC (D) (n = 7 mice) after each behavioral session. **(E)** Representative *in vivo* images of CA1 (upper panels) and the RSC (lower panels), showing the same fields of view after H, C, and R1–3. Cyan and magenta dots denote *Arc*+ neurons in CA1 and the RSC, respectively. Bottom, example images of a neuron with red arrows indicating *Arc* transcription sites. (**F**) *Arc*+ neurons in CA1 (top) and the RSC (bottom), colored by the number of times the neurons expressed *Arc*. **(G)** Overlap percentage of consecutively reactivated *Arc*+ neurons in CA1 and the RSC (* P < 0.05 by rank-sum test). **(H)** Venn diagrams of neurons that expressed *Arc* during CFC and re-expressed *Arc* during each retrieval test (left: CA1, right: RSC). Numbers indicate percentages of neurons. **(I)** The freezing rate is correlated with the overlap rate of *Arc*+ neurons in the RSC (magenta), but not in CA1 (cyan) (CA1: R = -0.40, P = 0.84, n = 8 mice; RSC: R = 0.52, P = 0.04, n = 12 mice; by Pearson's correlation). **(J-K)** Overlap percentage of *Arc*+ neurons at one- (left) or two-day intervals (right) (* P < 0.05, ** P < 0.01 by pairwise t test) in CA1 (J) and the RSC (K). **(L-M)** Overlap of *Arc*+ populations between CFC and context B conditions compared with chance levels in CA1 (L) and the RSC (M). Scale bars, (E and F) 50 μm and (E, bottom) 10 μm. Error bars represent SEM.

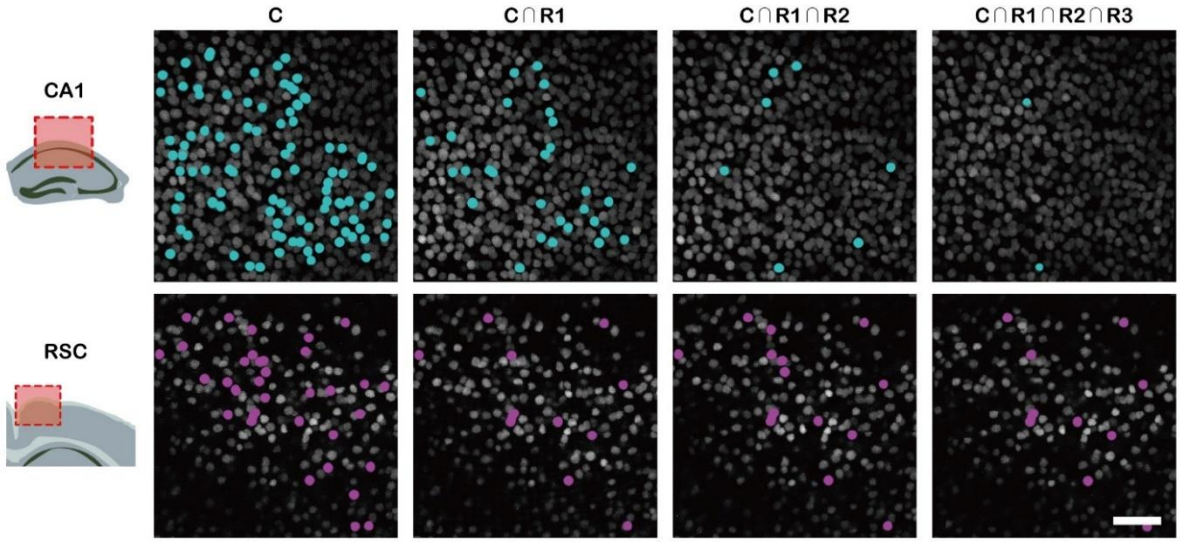

Fig. 3.2. Overlap of *Arc*+ neurons upon recent memory retrieval. Representative images of CA1 (upper panels) and the RSC (lower panels) showing overlapping populations of *Arc*+ neurons upon recent memory retrievals. (cyan dots, CA1; magenta dots, RSC). Scale bar, 50 μm.

3.2.2 Stability of overlapping *Arc*+ population in remote memory

To examine the stability of *Arc*+ neuronal ensembles at a longer time-scale, we performed repeated retrieval experiments on days 9, 16, 23, and 30 (Fig. 3.3A). All fear-conditioned mice showed freezing behavior during the remote memory retrieval tests (Fig. 3.3B). The fraction of *Arc*+ neurons in CA1 slightly decreased over a month (Fig. 3.3C), whereas the fraction in the RSC was similar (28–34%) for all sessions (Fig. 3.3D). The overlapping population of *Arc*+ neurons sharply decayed in CA1, but remained stable in the RSC for at least a month (Fig. 3.3E). Persistent *Arc* re-expression up to the fourth retrieval was observed in 4.0 ± 1.3% of the RSC neurons, but in almost none (0.2 ± 0.2%) of the CA1 neurons (Fig. 3.3F). The consecutive overlap of *Arc*+ neurons was significantly higher in the RSC than CA1 from R2 (Fig. 3.3G). The overlap between *Arc*+ populations elicited by memory retrieval at 1–4 weeks apart was

also mostly higher than chance levels in the RSC, but not in CA1 (Fig. 3.4). To visualize how *Arc*+ neurons turn over during remote memory retrievals, we used tree graphs to trace *Arc* re-expression probabilities (Fig. 3.3H). RSC neurons that consistently expressed *Arc* were more likely to be reactivated, in accordance with previous reports on neocortical IEG expression. However, in CA1, an almost random population of neurons expressed *Arc* whenever the mouse was re-exposed to the same context.

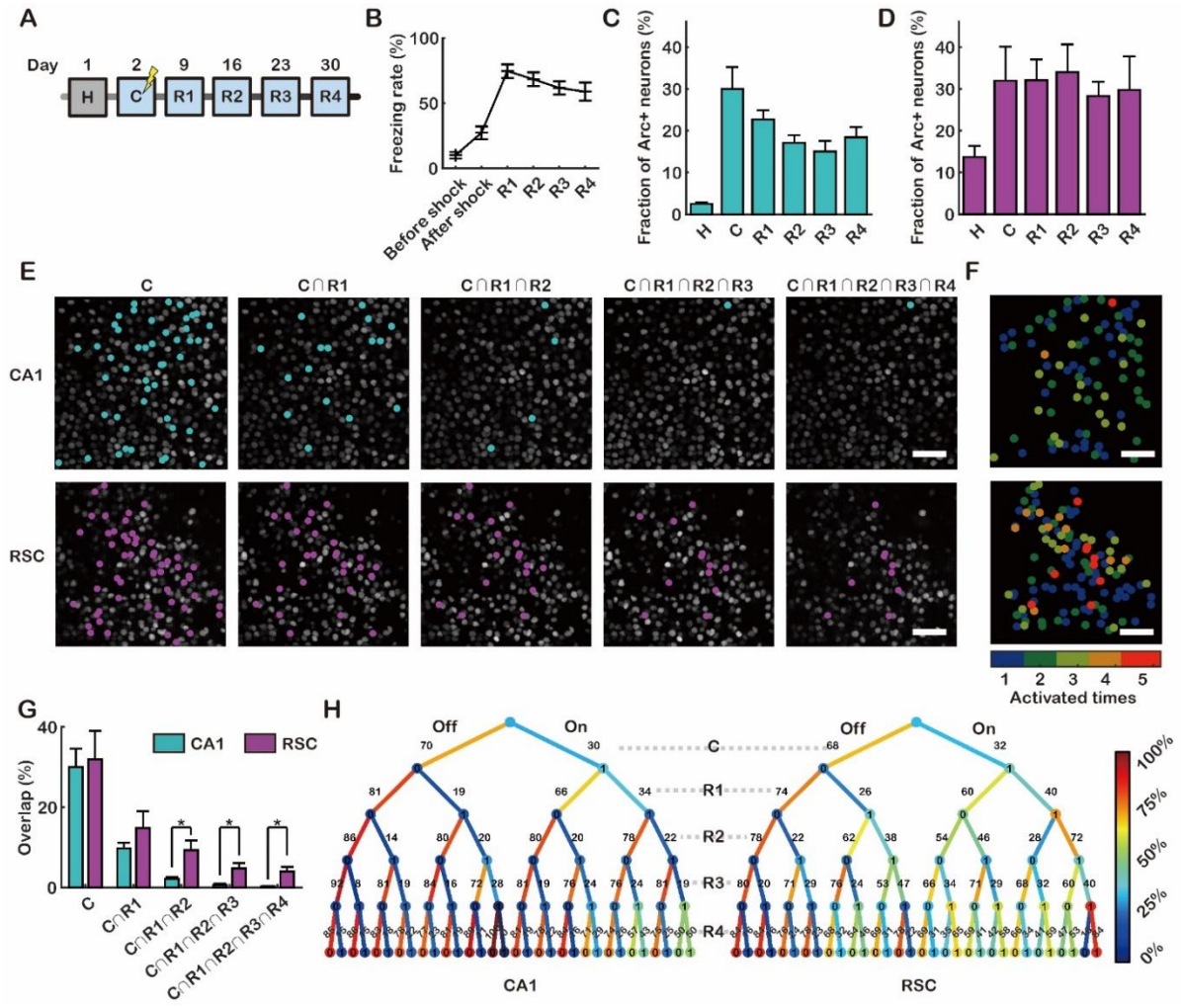

Fig. 3.3. Long-term dynamics of *Arc*+ neuronal ensembles in CA1 and the RSC. (A) Experimental scheme of remote memory retrieval tests. **(B)** Freezing rates of PCP×PBS mice during CFC and four retrieval tests (R1–4) (*n* = 8 mice). **(C-D)** The fraction of *Arc*+ neurons

in CA1 (C) (n = 4) and the RSC (D) (n = 4) after each session. (**E**) Representative images of CA1 (top) and the RSC (bottom) showing overlapping populations of *Arc*+ neurons (cyan, CA1; magenta, RSC). **(F)** *Arc*+ neurons in CA1 (top) and the RSC (bottom) labeled to reflect the number of *Arc* expression events. **(G)** The percentage of neurons that consecutively re-expressed *Arc* in CA1 (cyan) and the RSC (magenta) (* $P < 0.05$ by Student's t-test). (**H**) Tree graphs colored by the re-expression probability of neurons in CA1 (left) and the RSC (right). The first layer represents the fraction of neurons that expressed (rightwards) or did not express (leftwards) *Arc* upon CFC. The other layers are further split according to the presence or absence of *Arc* transcription sites upon retrieval. Scale bars, (E and F) 50 μm. Error bars represent SEM.

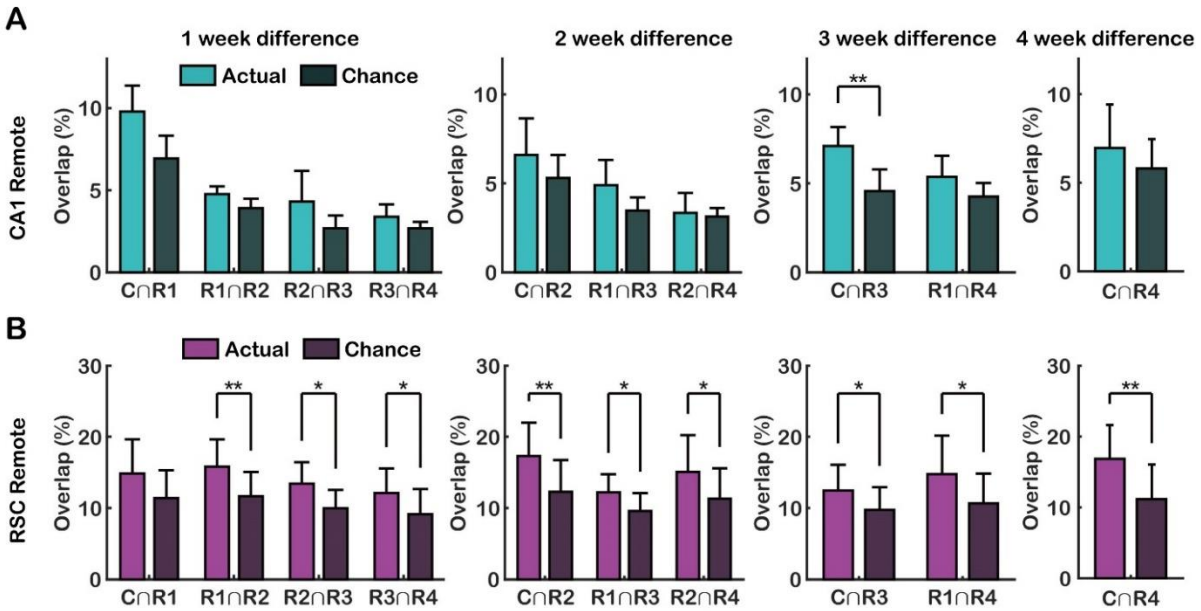

Fig. 3.4. Overlap between *Arc*+ populations after remote memory retrievals (A-B) The percent overlap between *Arc*+ ensembles in CA1 (A) and the RSC (B), with 1–4-week differences compared with the chance level (* $P < 0.05$, ** $P < 0.01$ by one-tailed pairwise t

test). RSC ensemble overlap was generally significantly greater than chance levels, whereas most CA1 ensembles exhibited chance-level overlap. Error bars represent SEM.

3.3 References

1. S. Tonegawa, M. D. Morrissey, T. Kitamura, The role of engram cells in the systems consolidation of memory. *Nat Rev Neurosci* **19**, 485-498 (2018).
2. S. A. Josselyn, S. Tonegawa, Memory engrams: Recalling the past and imagining the future. *Science* **367**, eaaw4325 (2020).
3. M. M. Milczarek, S. D. Vann, F. Sengpiel, Spatial Memory Engram in the Mouse Retrosplenial Cortex. *Curr Biol* **28**, 1975-1980 (2018).
4. T. P. Todd, D. J. Bucci, Retrosplenial Cortex and Long-Term Memory: Molecules to Behavior. *Neural Plast* **2015**, (2015).
5. D. J. Cai *et al.*, A shared neural ensemble links distinct contextual memories encoded close in time. *Nature* **534**, 115-+ (2016).
6. A. Rubin, N. Geva, L. Sheintuch, Y. Ziv, Hippocampal ensemble dynamics timestamp events in long-term memory. *Elife* **4**, (2015).

4. Neural activities of Arc+ neurons

4.1 Introduction

Recent advances of engram tagging technologies provided valuable information about the relation between neuronal ensemble and memory [*1*]. However, most of engram studies focused on the neuronal population involved in specific memory instead of their neural activity during memory encoding or memory testing. Recent paper from McHugh's group demonstrated tetrode recording of engram neurons in CA1 during exploration of novel environments [*2*]. They found the engram neurons has less spatial information compared to non-engram place cells and high theta frequency during encoding stage. However, the relation between IEG-positive neurons during the memory testing and their neural activities is unclear.

In chapter 3, we have observed the dynamic change of IEG-positive neuronal ensemble in CA1 both in recent and remote times. It is still not clear whether the neuronal ensemble that expressed Arc both encoding and retrieval is necessary for the specific memory. To investigate the neural activity of IEG-positive neurons in each day, in this chapter, I performed Arc transcription site imaging and calcium imaging while the mice is exploring the virtual reality (VR) environment. I installed the 6 monitors and a spherical treadmill on the two-photon excitation microscope, and imaged the CA1 neurons before and after the VR exploration.

The experiment was performed for 3 days. The mice were exposed to the virtual environment A, A, and B on day 1, 2, and 3, respectively. We found the Arc+ neurons had higher neural activities. The neurons that expressed Arc both during the memory encoding and the memory testing showed selectively high theta-burst rate, which suggest these population facilitate the memory by regulating the theta-burst. Lastly, we calculated the correlation between the

calcium traces and generated the network graph.

4.2 Materials and methods

4.2.1 Image analysis and calcium signal extraction

The image registration and data extraction process for the VR experiment included: 1) motion correction of the *Arc* mRNA images using NoRMCorre [*3*] and stackReg [*4*] software; 2) stitching two ROIs and subtracting auto-fluorescence; 3) alignment of images taken before and after VR and on different days; 4) matching the same field of view in *Arc* mRNA and calcium images; 5) obtaining nucleus centroid coordinates using Imaris software (Bitplane); 6) calcium source extraction using CaImAn software [*5*], which is based on a constrained non-negative matrix factorization (CNMF) algorithm by seeding the nucleus centroid locations as initial spatial components; and 7) matching the nucleus and spatial components detected by CaImAn finding the nearest centroid position.

To detect transcription sites that are near diffraction-limited spots, we needed a high signal-to-noise ratio, high spatial resolution, and little distortion from motion artifacts. For this, we acquired 45 images in each z-plane at 30 Hz and obtained the average image after image registration by x-y translation using NoRMCorre. The z-axis of the image was then aligned using StackReg software. Two ROIs were stitched using the stitching plugin in ImageJ software. To align stitched voxels taken in different days, we wrote a custom MATLAB script that finds overlapping voxels by calculating cross-correlations (Fig. S7). The calcium activity images were first corrected for motion artifacts by using NoRMCorre software. Cross-correlations were then calculated between the *Arc* mRNA images and averaged calcium images to find the same field of view and corresponding z-plane. To obtain the 3-dimensional coordinate of neuronal nuclei, we used the surface segmentation tool of Imaris (Bitplane) software. The locations of cells within 10 μm of the calcium imaging plane were used as the

initial spatial components in CaImAn software. After running CaImAn, the output spatial components were used to identify nuclear coordinates by finding the nearest neighbor centroid position. The calcium activity traces were calculated using the temporal component values from CaImAn, and relative changes (ΔF/F) were computed. The calcium trace baseline was selected manually and corrected for photobleaching. A calcium transient event was defined as an event starting from the moment ΔF/F exceeded three standard deviations (SD) of the baseline to the moment that ΔF/F returned to within 0.5 SD of the baseline. We considered cells with at least one calcium transient to be active cells. False-positive calcium transients due to motion artifacts in the z-axis were occasionally observed during murine grooming behavior. To remove these artifacts, we used the calcium activity data recorded only during walking (speed > 0.5 cm/s and run length > 0.5 cm). To resolve finer spiking activity, we deconvoluted ΔF/F traces and inferred the spike traces. Ca^{2+} event rates were calculated by dividing the sum of the inferred spikes by time. A burst was defined as spikes that were larger than a threshold value of 2.5 in a 33-ms time bin or continuous over multiple time bins. We defined theta-burst events as bursts occurred at interburst intervals of 100 to 166 ms (6 to 10 Hz) following a similar method in [*2*].

4.2.2 Virus injection

For virtual reality (VR) experiments, we injected 1 μl of 10^{13} vg/ml of AAV1-hSyn-NES-jRGECO1a (Addgene, #100854) into AP -2.0 mm, ML +1.8 mm and DV -1.4 mm from the bregma. Three days after virus injection, hippocampal window surgery was performed. The injection was made using a 33-gauge needle connected to a Hamilton syringe and mounted on a micro-injection pump (Harvard Apparatus, Pump 11 Pico Plus Elite). The cranial window surgery was

performed as described in chapter 2.

4.2.3 Virtual reality experiment and imaging

Water restriction and training were performed before VR experiments. Water restriction (1 ml/day) was applied for 5 days using a water dispenser connected to a multi-channel syringe pump (New Era, NE-1600). VR experiments were performed using the JetBall-TFT system (Phenosys), which consists of a 270° 6-panel monitor, a spherical treadmill, and a water reward device. To restrict the spherical treadmill movement to one dimension, a needle was inserted on one side of the treadmill. After 5 days of water restriction, training was performed on an infinite virtual linear track for 0.5~1 hour per day for 10-14 days, and water rewards were delivered at random positions. Mice were subjected to experimentation on the day following their demonstrated capability to travel longer than 50 m in 30 min. On experimental days 1 and 2, mice were exposed to virtual Context A (Fig. 4B) which was 3 m long, 0.4 m wide, and consisted of buildings and moon objects. On day 3, mice were placed into virtual Context B which was 3 m long, 1 m wide, and made up of objects and wall patterns different from Context A. After reaching the end of the track, the mice were teleported to the starting point. To induce a perception of movement on a continuous track, tunnels were placed at the front and the end of the virtual contexts. Water reward was delivered at the end of each tunnel.

For *Arc* transcription and calcium imaging in virtual reality experiments, mice were mounted on the microscope while awake. *Arc* transcription imaging was performed for ~3 min before and after the VR experiment. We imaged 2 ROIs with a volume of 128 μm × 128 μm × 20 μm using a resonance scanner. During the virtual reality experiment, calcium activity was observed via jRGECO1a signal. Images of 256 μm × 256 μm areas were acquired at 30 Hz using a resonance scanner. Calcium imaging was initiated by triggering a signal from JetBall software

to simultaneously record VR positions and calcium activity. After the VR experiment, we immediately anesthetized the mice to prevent additional stimulation, and re-imaged the ROI.

4.2.4 Fixed brain imaging

To image jRGECO1a in fixed brain tissues, we used a wide-field fluorescence microscope (Olympus, IX83) equipped with a 20× 0.5 NA objective (Olympus, UPLFLN20X), a motorized stage (Marzhauser), and an EMCCD camera (Andor iXon Life 888). To obtain a large field of view, we performed 15 × 18 grid imaging and stitched the images after shading correction using BaSiC software [*6*].

4.2.5 Place cell identification

Place cells were defined using a method similar to an approach described previously [*7*]. The 3-m-long virtual track was first divided into 150 position bins (2 cm per bin). Using the ΔF/F traces obtained during running (speed >1.5 cm/s and run length > 5 cm), we calculated the sum of ΔF/F for each bin and normalized by the dwell time in each bin to generate a ΔF/F field map. The resulting ΔF/F field map was smoothed by computing the moving average with a sliding window of three bins. The potential place field was identified as a region exceeding the median value of the ΔF/F field map. Place cells were then identified using the following criteria: 1) the potential field is wider than 20 cm; 2) the mean value of the ΔF/F field map in the potential field must be 2.2 times higher than the mean value of the ΔF/F field map outside the potential field; and 3) Ca^{2+} events must be present in at least 15% of the visits to the potential field. To evaluate whether each mouse actually distinguished virtual Contexts A and B, we calculated spatial correlation. For neurons identified as place cells on day 1, we calculated the Pearson's correlation coefficient of the ΔF/F field map between the same or different contexts. The spatial

information was calculated using the following formula [*8*]:

$$\text{Spatial information} = \sum_i \frac{\lambda_i}{\lambda} \log_2 \frac{\lambda_i}{\lambda} P_i$$

where λ is the Ca^{2+} event rate, λ_i is the mean Ca^{2+} event rate in the ith place bin, and P_i is the probability that the mouse stays in the ith place bin.

4.2.6 Network graph

We first converted the Ca^{2+} event traces into binary and temporally binned (1 sec per bin) traces. The resulting traces were used to generate a correlation matrix by calculating Pearson's correlation coefficients. We then generated a binary adjacent matrix with pairs that were statistically significant ($p < 0.05$) and had a correlation coefficient higher than 0.1. The network graph was visualized using Gephi (https://gephi.org/) software with the ForceAtlas2 layout. We calculated degrees, cluster coefficients, and modularity using custom written MATLAB scripts. The degree k_v denotes the number of edges in each neuron. The normalized degree was calculated by dividing k_v by (the number of neurons in network -1). Clustering coefficients were calculated using the following formula [*9*]:

$$C_v = \frac{\sum_{j,k} A_{vj} A_{jk} A_{kv}}{k_v(k_v - 1)}$$

where A is the adjacent matrix in which A_{ij} is a binary value indicating whether the ith neuron and the jth neuron are correlated. The normalized modularity was calculated using the following formula [*10*]:

$$Q_{normalized} = \frac{Q}{Q_{max}} = \frac{\sum_{i,j} \left(A_{ij} - \frac{k_i k_j}{2m} \right) \delta(t_i, t_j)}{2m - \sum_{i,j} \frac{k_i k_j}{2m} \delta(t_i, t_j)}$$

where m is the number of edges in the network, t_i denotes the module (*Arc*++/non-*Arc*++ or

place cell/non-place cell) of the ith neuron, and δ is a delta function.

4.3 Results and Discussion

4.3.1 Calcium activity of *Arc*+ neurons during VR navigation

Given our data on the high turnover rate of *Arc*+ neurons in CA1, we wanted to investigate the neuronal activity of these cells during memory encoding and retrieval. To monitor calcium activity of *Arc*+ neurons, we performed dual-color imaging of CA1 in head-fixed awake mice running on a trackball to navigate a virtual reality (VR) linear track (Fig. 4.1A). We injected adeno-associated virus (AAV) expressing the red genetically-encoded calcium indicator (GECI) jRGECO1a [*11*] into the dorsal CA1 of PCP×PBS mice (Fig. 4.2). Six mice were exposed to a novel context (ctx A) on day 1 and again on day 2, followed by a distinct context (ctx B) on day 3 (Fig. 4.1B). On each day, we imaged *Arc* mRNA in awake resting state, calcium activity during VR navigation, and *Arc* mRNA under anesthesia (Fig. 4.1C, and Fig 4.3). The fraction of neurons with *Arc* transcription sites significantly increased after VR navigation on each day (Fig. 4.1D). Cells that transcribed *Arc* after VR navigation on day 1, 2, and 3 were referred to as A1-*Arc*+, A2-*Arc*+, and B-*Arc*+ neurons, respectively. The calcium activity of the *Arc*+ neurons was similar with or without prior transcription of *Arc* before VR navigation (Fig. 4.4). The overlap between the three *Arc*+ populations was 15–17% (Fig. 4.1E)—significantly higher than chance levels (Fig. 4.6). We compared the calcium activity of *Arc*+ and *Arc*- neurons pooled from all three sessions. The calcium trances were deconvolved to spike trains, from which we calculated the 'inferred burst' and 'inferred theta-burst' (6-10 Hz) rates (Fig. 4.4). By applying the same analysis on cultured neurons under electrical stimulations, we confirmed that burst activity at a frequency of 6-10 Hz could be detected by the deconvolution algorithm (Fig. 4.5). Although almost all neurons (99.9%) showed varying degrees of activity (Fig. 4.1F), *Arc*+ neurons were significantly more active than *Arc*- neurons on average (Fig. 4.1G).

4.3.2 Calcium activity of *Arc*+ neurons during VR navigation

We next identified place cells on each day and calculated the spatial correlation between place fields (Fig. 4.1H and Fig. 4.7A-C). The correlation between place fields in the same context (A-A) was significantly higher than in different contexts (A-B), indicating that the mice perceived the two virtual environments as different contexts (Fig. 4.7D). Among the place cells, A1-*Arc*+ neurons showed lower spatial correlations between days 1 and 2 than A1-*Arc*- neurons (Fig. 4.7E). A1-*Arc*+ neurons also had lower spatial information than A1-*Arc*- neurons on day 1 (Fig. 4.1I), consistent with a previous report on *c-Fos*-positive neurons. These results support that the IEG-positive CA1 neurons do not necessarily represent spatial information about the context [*2*].

4.3.3 Calcium activity of *Arc*+ neurons during VR navigation

To further dissect the activity of *Arc*+ neurons, we grouped the CA1 neurons into eight subpopulations shown in Fig. 4E and compared their calcium activity on each day (Fig. 4.1J and Fig.4.8A). Neurons that transcribed *Arc* on both day 1 and 2 (*Arc*++) had higher inferred theta-burst activity (6-10 Hz) in ctx A than ctx B (Fig. 4.1J and K). Neurons that expressed *Arc* on day 1 but not day 2 (*Arc*+-) showed a similar inferred theta-burst rate as neurons that did not express *Arc* on either day (*Arc*--). These data suggest that only *Arc*++ neurons may be involved in the engram for ctx A through relatively high inferred theta-burst activity during both encoding and retrieval. Interestingly, neurons that expressed *Arc* on all three days (*Arc*+++) also showed significantly higher inferred theta-burst rates in ctx A than ctx B (Fig. 4.1J and L), indicating that these neurons are part of the engram for ctx A but not ctx B. On the other hand, neurons that expressed *Arc* only on days 2 and 3 (*Arc*-++) showed a high inferred theta-burst rate on day 3 (Fig. 4.1J and L). These results indicate that only a subpopulation of IEG-positive neurons may represent an engram for a specific memory.

4.3.4 Calcium activity of *Arc*+ neurons during VR navigation

We then examined whether these putative engram *Arc*++ neurons were simultaneously reactivated during memory retrieval as in optogenetic experiments. The correlation coefficient among the *Arc*++ neurons was similar to those among the non-*Arc*++ neurons (Fig. 4.7B and C). After calculating the correlation coefficient matrices, we generated network graphs of correlated neuronal activity on each day (Fig. 4.1M). The network properties were quantified using the number of correlated pairs (degree), the fraction of pairs among neighbors (clustering coefficient) [*9*], and the strength of division of the network into modules (modularity) [*10*]. *Arc*++ neurons showed a higher normalized degree and clustering coefficient in ctx A than ctx B (Fig. 4.1N), indicating highly correlated activity with other CA1 neurons during encoding and retrieval of a contextual memory. The modularity of *Arc*++ neurons was close to zero (Fig. 4.1O), which suggests that they are integrated with rather than segregated from other neurons in CA1. Meanwhile, place cells identified each day showed higher modularity than *Arc*++ neurons (Fig. 4.1O) and formed a dense cluster on day 2 (Fig. 4.1M), in line with a previous report. These results suggest that *Arc*++ neurons have memory-specific connectivity but do not necessarily have synchronized inputs.

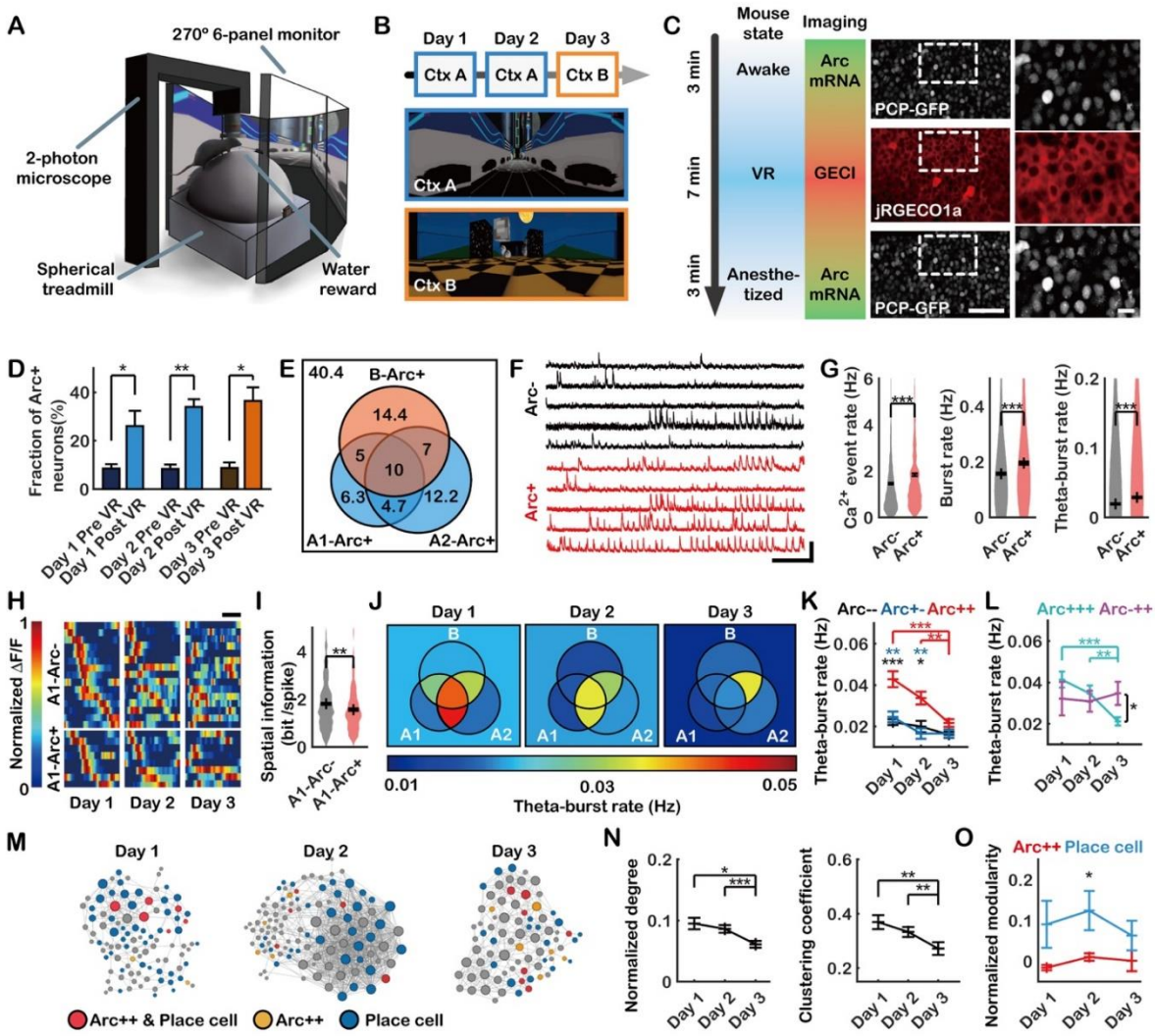

Fig. 4.1. *Arc* transcription and calcium imaging in CA1 of mice exploring virtual reality (VR). (A) Experimental setup. **(B)** Experimental schedule (top) and virtual context A (middle) and B (bottom). **(C)** *Arc* transcription imaging was first conducted while mice were awake, followed by calcium imaging while exploring VR. After 7 min of exploration, *Arc* transcription imaging was performed under anesthesia. Representative images and magnified insets shown at right. **(D)** Fractions of neurons with *Arc* transcription sites before and after VR on each day (* $P < 0.05$, ** $P < 0.01$ by pairwise *t* test, $n = 6$ mice). **(E)** A Venn diagram of *Arc*+ neurons on days 1, 2, and 3. **(F)** Representative calcium traces of *Arc*- and *Arc*+ neurons. **(G)** Left, Ca^{2+} event rates of *Arc*- and *Arc*+ neurons (*** $P < 10^{-8}$ by rank-sum test). Middle, burst rates of

Arc- and *Arc*+ neurons (*** $P < 10^{-10}$ by rank-sum test). Right, inferred theta-burst rates of *Arc*- and *Arc*+ neurons (*** $P < 10^{-19}$ by rank-sum test; Arc^{-}: n = 1085 neurons, Arc^{+}: n = 651 neurons). **(H)** An example of place fields of place cells that are A1-*Arc*- (top) or A1-*Arc*+ (bottom) neurons on days 1, 2 and 3. Neurons were ordered by the maximum value locations of the place field on day 1. **(I)** Spatial information of A1-*Arc*- and A1-*Arc*+ neurons on day 1 (** $P < 0.01$ by rank-sum test; A1-*Arc*-: n = 430 neurons, A1-*Arc*+: n = 209 neurons). **(J)** Venn diagrams of average *Arc*+ neuron inferred theta-burst rates on days 1, 2 and 3. **(K)** Inferred theta-burst rates of *Arc*--, *Arc*+- and *Arc*++ neurons on each day (* $P < 0.05$, ** $P < 0.01$, *** $P < 10^{-4}$ by Student's t test; *Arc*--: n = 261-302 neurons, *Arc*+-: n = 69-92 neurons, *Arc*++: n = 103-116 neurons). **(L)** Inferred theta-burst rate of *Arc*-++ and *Arc*+++ neurons on each day (* $P < 0.05$, ** $P < 0.01$, *** $P < 10^{-4}$ by Student's t test; *Arc*-++: n = 36-47 neurons, *Arc*+++: n = 65-81 neurons). **(M)** An example of network graphs of a mouse on days 1, 2 and 3. Nodes are classified by color, and their size is proportional to the degree of the neurons. **(N)** Normalized degree (left) and clustering coefficient (right) of *Arc*++ neurons on each day (* $P < 0.05$, ** $P < 0.01$, *** $P < 10^{-4}$ by rank-sum test; n = 103-116 neurons). **(O)** Normalized modularity when dividing neurons into place cells and non-place cells (blue) and dividing neurons into *Arc*++ and non-*Arc*++ (red) (* $P < 0.05$ by Student's t test; n = 6 mice). Scale bars, (C, middle) 50 μm, (C, right) 10 μm, (F, horizontal) 1 min, (F, vertical) 150% ΔF/F and (H) 1 m. Error bars represent SEM.

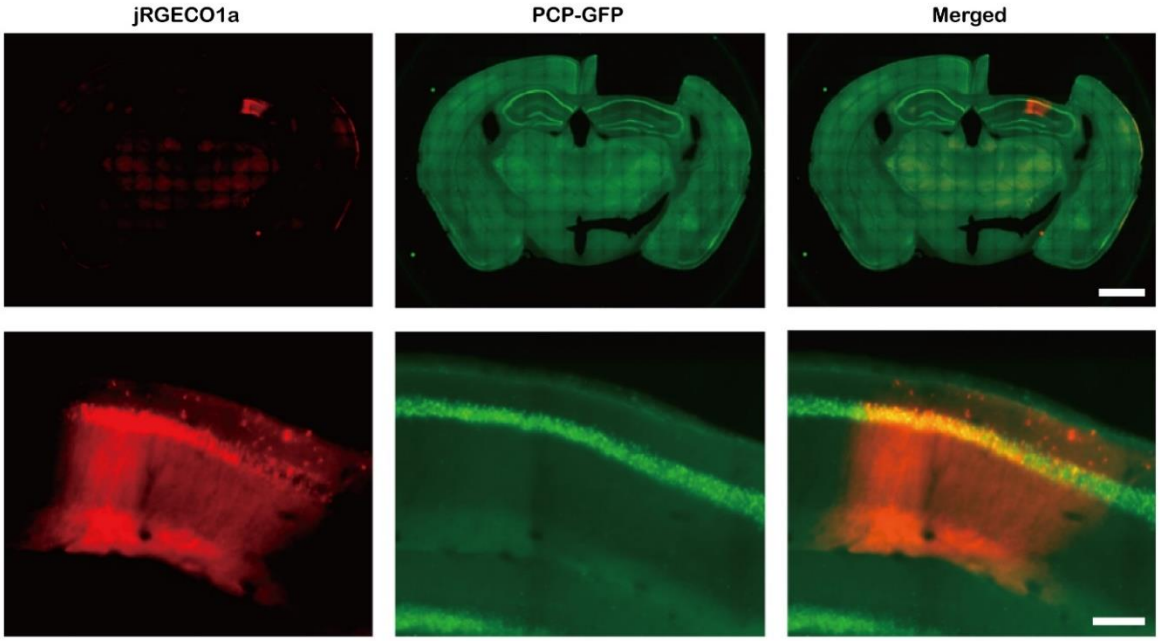

Fig. 4.2. Expression of jRGECO1a in CA1 of PCP×PBS mouse. AAV1-hSyn-NES-jRGECO1a was injected into the dorsal CA1 of PCP×PBS mice**.** Coronal section images of the dorsal CA1 pyramidal cell layer expressing jRGECO1a (red) and PCP-GFP (green). Scale bars, (upper panel) 1 mm and (lower panel) 100 μm.

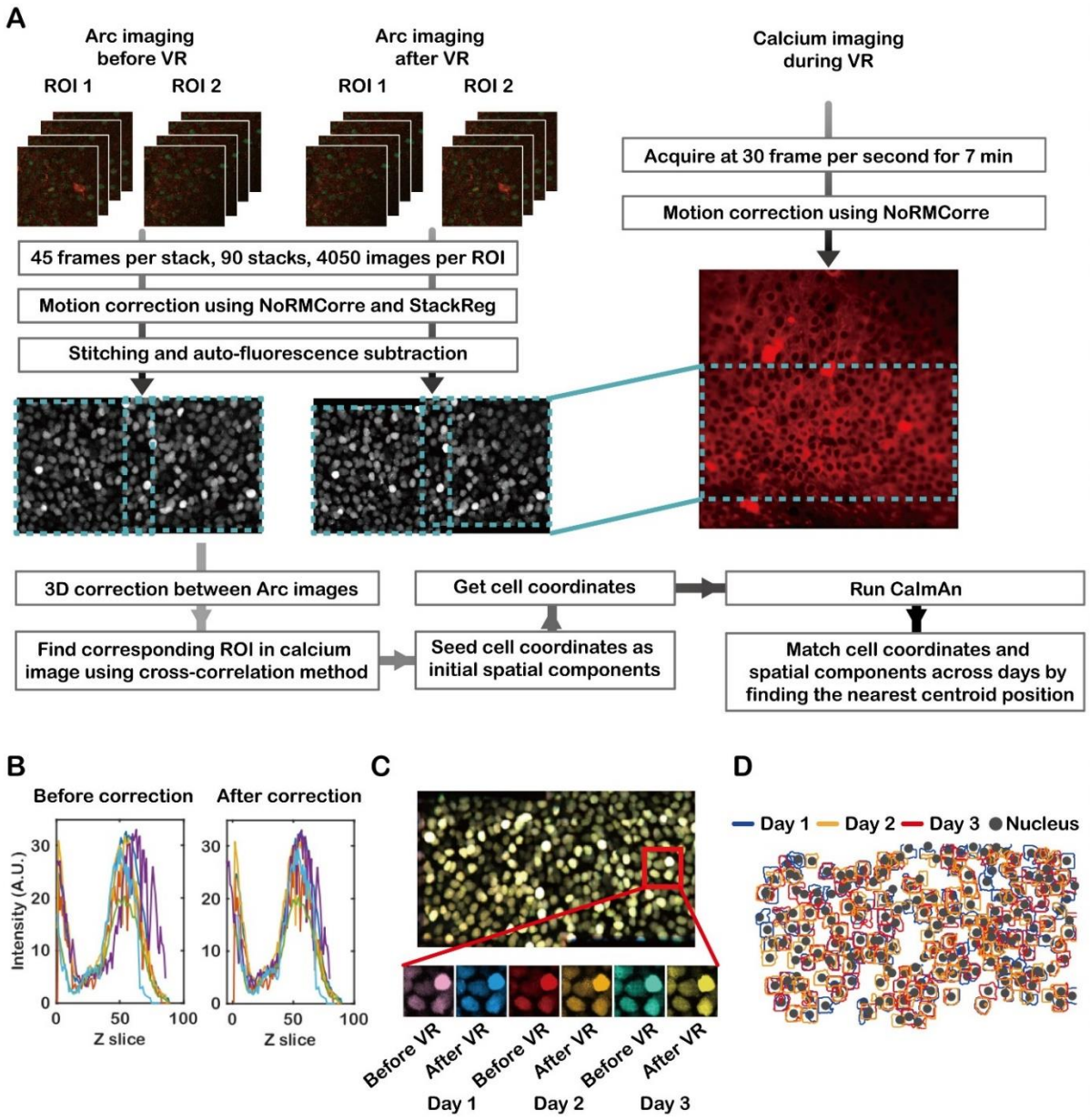

Fig. 4.3. Image registration pipeline for *Arc* mRNA and calcium images. (A) Raw images of *Arc* mRNA were first corrected for motion artifacts, followed by ROI stitching, auto-fluorescence subtraction, correction across days, and cell coordinate detection. Calcium images were corrected for motion artifacts, and calcium footprints were detected using constrained non-negative matrix factorization (CNMF) with information of detected cells (see Methods for details). **(B)** A z-slice profile of *Arc* mRNA images before (left) and after correction (right). **(C)** Corrected images of *Arc* mRNA across multiple days. **(D)** Identified spatial footprints

using CNMF over multiple days. Cell coordinates and spatial footprints were matched by finding the nearest centroid position.

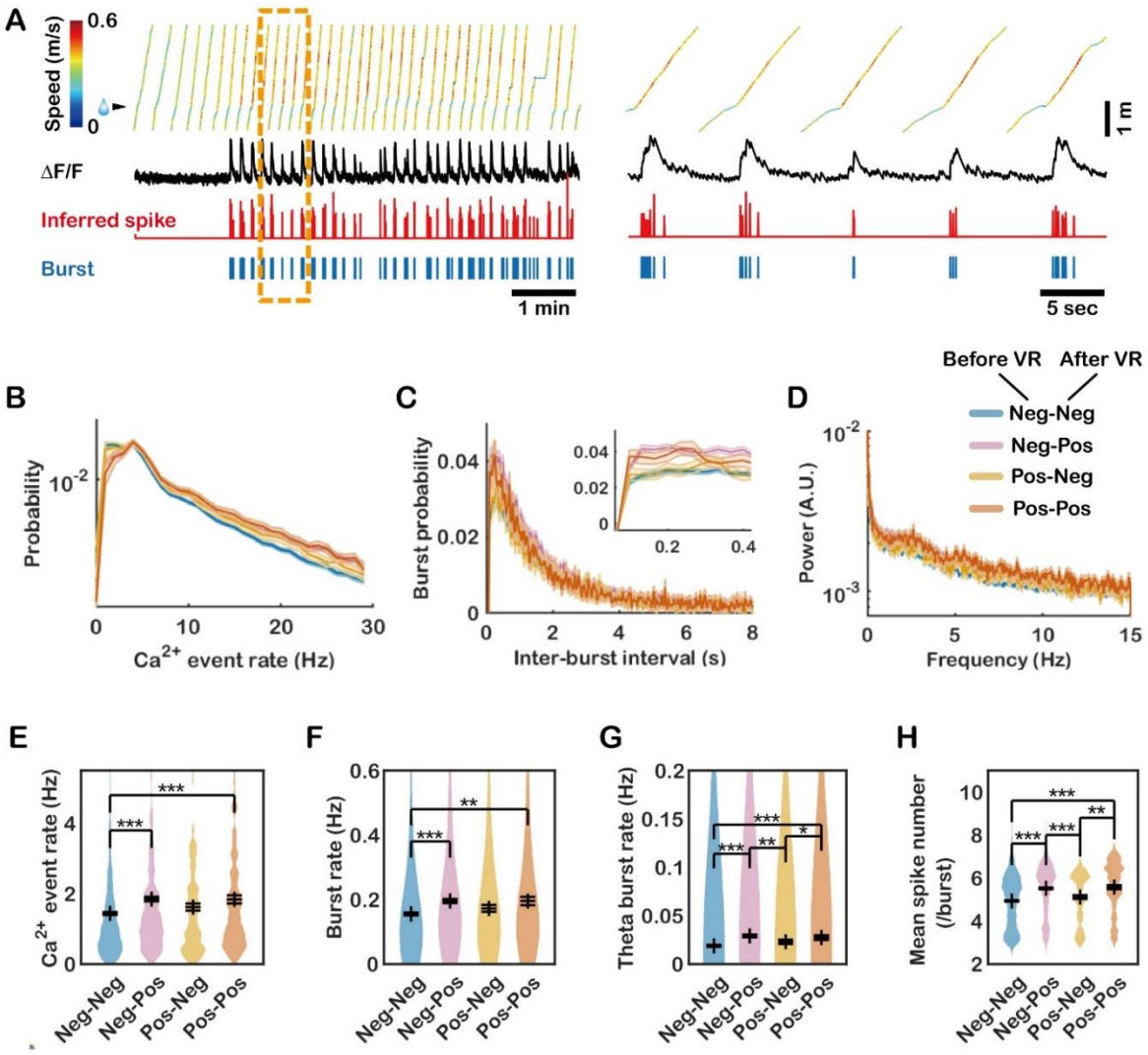

Fig. 4.4. Calcium activity of CA1 neurons during VR navigation. (A) An example of the VR track position with the colormap of the running speed over time. A representative neuron's calcium trace, inferred spike trace from deconvolution, and burst trace are shown at the bottom (left). A segment of traces in the yellow dashed box is magnified at right. **(B-D)** We classified neurons into four classes according to neuronal transcription of *Arc* mRNA before and after VR. The Ca^{2+} event rate histogram (B), autocorrelation (C), and power

spectrum (D) of each class were plotted. **(E-H)** The Ca^{2+} event rate, burst rate, theta-burst rate, and mean spike number per burst of each group were plotted (* $P < 0.05$, ** $P < 0.01$, *** $P < 10^{-10}$ by rank-sum test). Generally, neurons in the Neg-Pos group had similar activity properties to neurons in the Pos-Pos group. Error bars represent SEM.

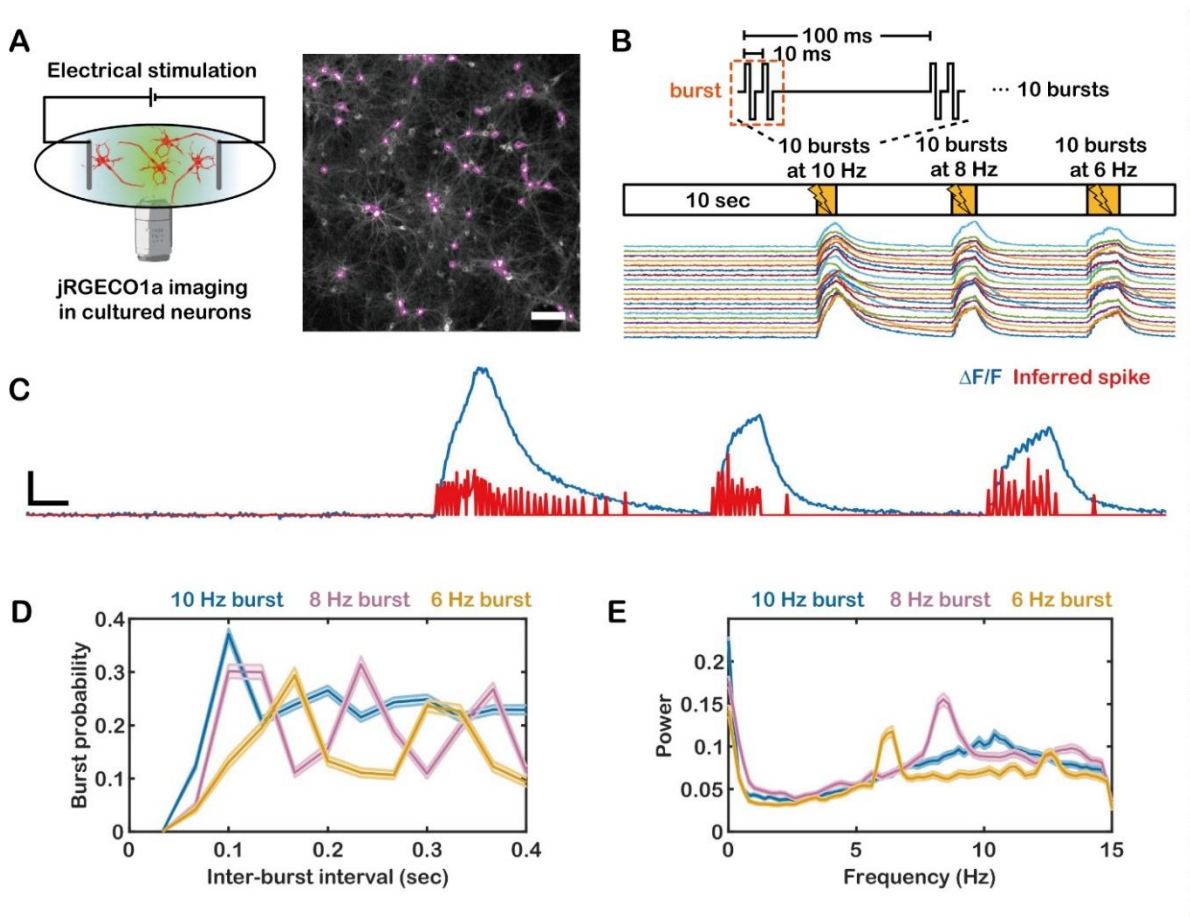

Fig. 4.5. Calcium imaging of primary cultured hippocampal neurons upon 6~10 Hz burst electrical stimulations. (A) Experiment scheme of electrical stimulation (left) and a representative image of cultured neurons expressing jRGECO1a (right). Magenta contours represent the ROIs for calcium fluorescence signals. **(B)** A single burst contains two electrical pulses with 10 ms interval. 10 bursts were delivered to neurons at 10, 8, and 6 Hz interspaced by 7 s. The calcium trace ΔF/F of 20 representative neurons are shown at the bottom. **(C)** An example of ΔF/F trace and inferred spike trains. **(D)** Histogram of the inter-burst intervals during 10, 8, and 6 Hz stimulations. **(E)** Power spectra of bursts during 10, 8, and 6 Hz

stimulations. Scale bars, (A) 100 µm, (C, vertical) 500% ΔF/F and (C, horizontal) 1 s.

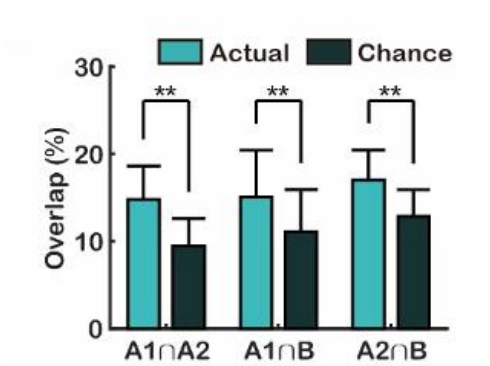

Fig. 4.6. Comparison of overlap rates with chance levels. Overlap between *Arc*+ neurons identified on days 1, 2, and 3 compared with chance levels (** $P < 0.01$, by pairwise *t* test). Error bars represent SEM.

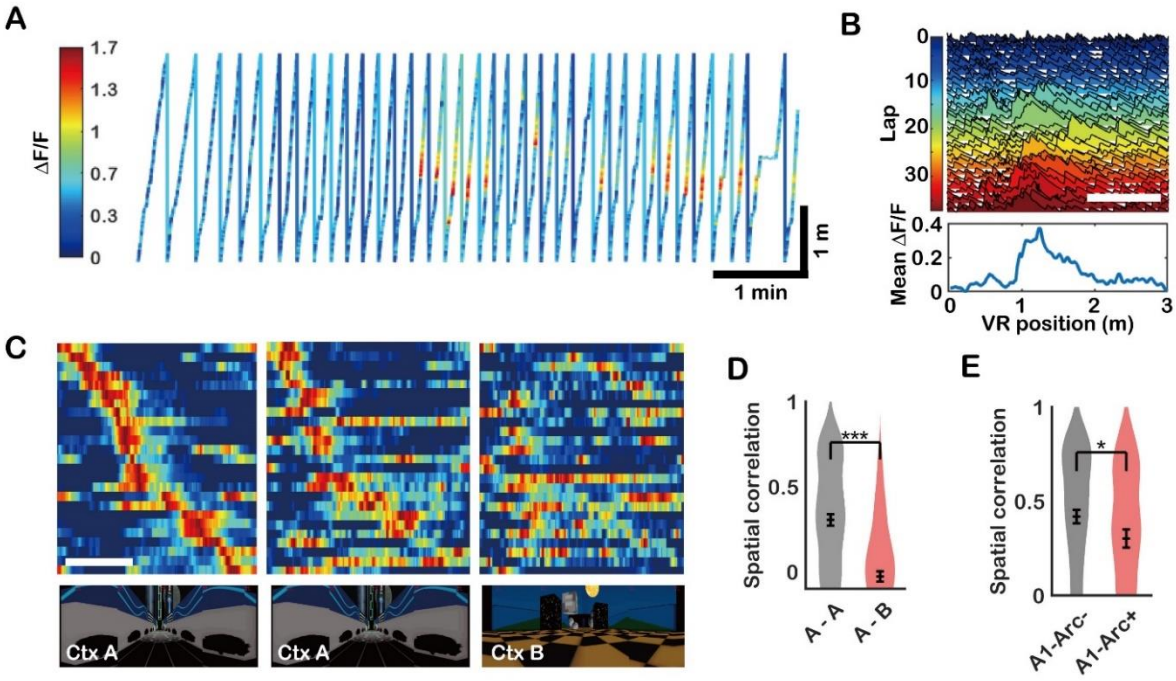

Fig. 4.7. Spatial correlation after exposure to the same or different virtual contexts. (A) Position versus time plot of a mouse running along the virtual linear track, colored according to ΔF/F values of a representative place cell. **(B)** Joyplot showing the calcium traces of each lap and the mean calcium trace of the place cell shown in (A). **(C)** Mean place fields on days

1–3, sorted by place cells detected on day 1. **(D)** Spatial correlation between place fields when mice were exposed to the same (A-A) or different (A-B) contexts. **(E)** Comparison of A1-*Arc*- and A1-*Arc*+ neurons in terms of their spatial correlation between place fields when mice were exposed to the same (A-A) contexts. Scale bar, (C) 1 m.

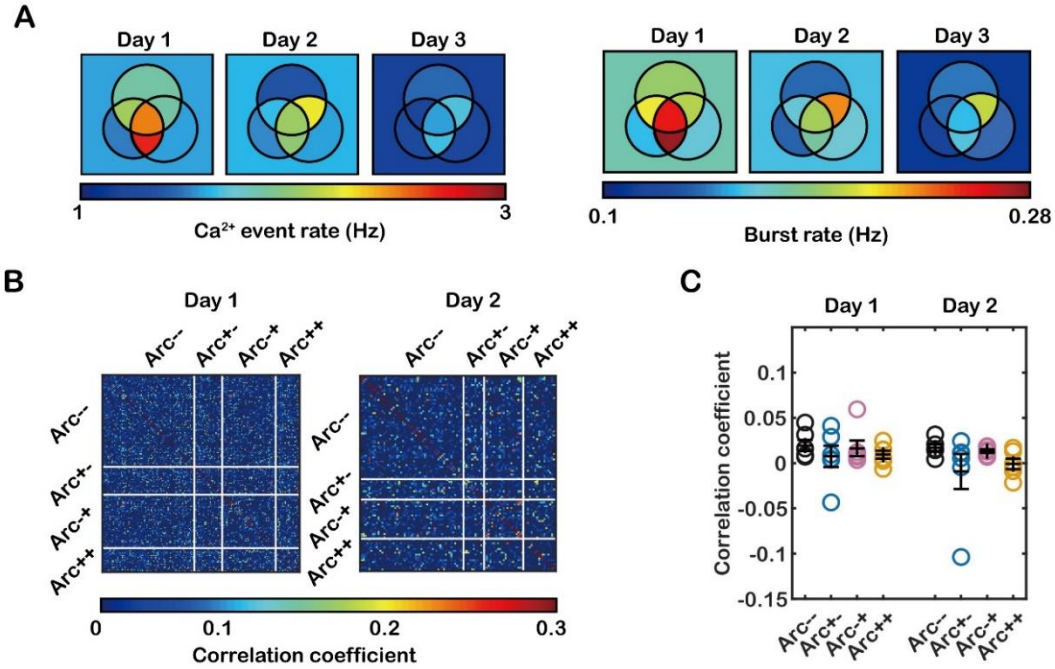

Fig. 4.8. Ca^{2+} event rates, burst rates and correlation coefficients of *Arc*+ subpopulations. **(A)** Venn diagrams of *Arc*+ neurons on days 1, 2, and 3 colored by the Ca^{2+} event rate (left) and the burst rate (right). **(B)** Correlation matrices generated by calculating the Pearson's correlation coefficient between binned spike traces. The neurons were arranged in the order of Arc--, Arc+-, Arc-+ and Arc++ neurons. **(C)** The correlation coefficient of the binned spike traces of the neurons in each group (n = 6 mice).

4.4 References

1. S. A. Josselyn, S. Tonegawa, Memory engrams: Recalling the past and imagining the future. *Science* **367**, eaaw4325 (2020).
2. K. Z. Tanaka, T. J. McHugh, The Hippocampal Engram as a Memory Index. *J Exp Neurosci* **12**, (2018).

3. E. A. Pnevmatikakis, A. Giovannucci, NoRMCorre: An online algorithm for piecewise rigid motion correction of calcium imaging data. *J Neurosci Meth* **291**, 83-94 (2017).
4. P. Thevenaz, U. E. Ruttimann, M. Unser, A pyramid approach to subpixel registration based on intensity. *Ieee T Image Process* **7**, 27-41 (1998).
5. A. Giovannucci *et al.*, CaImAn an open source tool for scalable calcium imaging data analysis. *Elife* **8**, (2019).
6. T. Y. Peng *et al.*, A BaSiC tool for background and shading correction of optical microscopy images. *Nature Communications* **8**, (2017).
7. D. A. Dombeck, C. D. Harvey, L. Tian, L. L. Looger, D. W. Tank, Functional imaging of hippocampal place cells at cellular resolution during virtual navigation. *Nat Neurosci* **13**, 1433-1440 (2010).
8. B. L. M. W. E. Skaggs, K. M. Gothard, E. J. Markus, An information-theoretic approach to deciphering the hippocampal code. *in Advances in Neural Processing Systems* **5**, 1030-1037 (1993).
9. D. J. Watts, S. H. Strogatz, Collective dynamics of 'small-world' networks. *Nature* **393**, 440-442 (1998).
10. M. E. J. Newman, Modularity and community structure in networks. *P Natl Acad Sci USA* **103**, 8577-8582 (2006).
11. H. Dana *et al.*, Sensitive red protein calcium indicators for imaging neural activity. *Elife* **5**, e12727 (2016).

5. Axonal mRNA dynamics in live neurons

5.1 Introduction

The localization of mRNA in the neuronal sub-compartment allows neurons to respond upon extracellular signals through the spatiotemporally regulated local protein synthesis [*1*]. In axons, which grow a long distance from soma, transporting mRNA is important for axonal navigation, branching and maintenance [*2*]. Since the local translation is a critical factor of the local proteome in neurites, a proper targeting of mRNA is required. Though several intracellular transport mechanisms of mRNA have been observed in different systems [*3, 4*], the molecular mechanism of how axonal mRNAs can localize to specific regions is unclear.

mRNAs are recruited to ribonucleoproteins (RNP) which is a package of mRNAs and proteins and RNPs directly associate with multiple motor proteins so that RNA can be transported [*5, 6*]. The specific motor protein composition of RNP is thought to create a mRNA localization pattern for proper functioning. Especially, the β-actin mRNA has a cis-acting element in the 3' untranslated region (UTR) which is recognized by zipcode-binding protein1 (ZBP1, the homolog of Vg1RBP and IMP-1). The β-actin RNP is transported by KIF5A and MYO5A and reported to localize at dendritic spines, axonal growth cone and axonal branching points [*7-9*]. In dendrite, the β-actin RNPs have been reported to follow the aging Lévy walk, which is an efficient strategy to find randomly located targets [*10*]. In axons, the localization of β-actin RNPs in growth cones was explained by a mathematical model which was established from anterograde/retrograde bias of β-actin mRNA [*7*].

One way to elucidate the localization mechanism of mRNA in axons is by tracking mRNAs in the live axon. Recent advances in mRNA labeling system allows to visualize single mRNAs in live neurons [*5, 11*]. Using the molecular beacon labeling of endogenous mRNA and

electroporating fluorescence dye-UTP labeled exogenous mRNA, recent studies demonstrated the visualization of single β-actin RNPs and analyzed motion types in axonal shaft and growth cone [*7, 12*]. However, real-time visualization of β-actin mRNA localization in branches was not performed yet. Furthermore, most of the studies were performed on the peripheral nervous system (PNS) neurons or retinal neurons of Xenopus [*1*], the localization pattern and the role of β-actin mRNA in the axon of hippocampal neurons is poorly understood.

Here, to visualize the β-actin mRNA in live axons, we employed a transgenic knock-in mouse, called MCPxMBS mouse, in which all endogenous β-actin mRNA is labeled up to 48 GFPs [*13*]. We report that the β-actin mRNA moves less motile and slower in axons than in dendrites. Along the axon, β-actin mRNAs showed different motion types according to different sub-compartments of the axon. In the axon shaft, the β-actin mRNA often showed transport state, while confined diffusion in filopodia and boutons. We further demonstrated that β-actin mRNAs were likely to localize at F-actin dense regions, so-called 'actin patch (AP)'. We analyzed the movement of β-actin mRNAs with and without AP. We found that the β-actin mRNAs dock to the AP and the confined diffusion of β-actin mRNAs were observed within APs.

5.2 Materials and methods

5.2.1 Microfluidic device fabrication

Microfluidic devices are fabricated by soft lithography. The master with positive relief features of negative photoresist SU-8 (MicroChem) was developed on 4 inch silicon wafer by photolithography, which is mold to reproduce the same device. A 10:1 (w/w) Polydimethylsiloxane (PDMS, Sylgard 184, Dow Corning) and curing agent was mixed gently and poured on the master. After degassing in a vacuum chamber to remove bubbles about 20 min, the mold is thermally cured on a hot plate to obtain replica molds. The reservoir parts for

the cell culture medium were punched out with biopsy punch (6 mm). After oxygen plasma for 60 sec to bond between PDMS molds and cover glass, the device is incubated in an 80°C dry oven at least 48 hours to maintain hydrophobic condition. The device is sterilized by UV irradiation before the experiment.

5.2.2 Primary mouse neuron cultures and transfection

All animal experiments were conducted by using a method approved by the Institutional Animal Care and Use Committee (IACUC) at Seoul National University. Primary hippocampal neurons were cultured from 1-day-old MCP×MBS mice pups, using a method described previously. Briefly, hippocampi were dissected out from the brains of 3-4 pups and dissociated by trypsin. For culturing on microfluidic devices, the microfluidic devices were coated with poly-D-lysine (10 mg/ml) for at least 6 hours and $2*10^5$ neurons were seeded. For culturing on glass-bottom dishes, dishes were coated with poly-D-lysine (2 mg/ml) and ~10^5 dissociated neurons were seeded. The neuron cultures were grown for 8-14 days in vitro in Neurobasal-A medium (Gibco) supplemented with B-26 (Gibco), Glutamax (Gibco), and Primocin (Invivogen) at 37°C and 5% CO_2.

5.2.3 Imaging single mRNA in live neurons

Live neuron imaging experiments were performed as described previously. Prior to imaging, culture medium was removed from the neuron culture and replaced with HEPES-buffered saline (HBS) containing 119 mM NaCl, 5 mM KCl, 2 mM $CaCl_2$, 2 mM $MgCl_2$, 30 mM D-glucose, and 20 mM HEPES at pH 7.4. The fluorescence images were taken by using U Apochromat 150× 1.45 NA TIRF objective (Olympus) on an Olympus IX73 inverted microscope equipped with two iXon Ultra 897 electron-multiplying charge-coupled device

(EMCCD) cameras (Andor), an MS-2000 XYZ automated stage (ASI), and Chamlide TC top-stage incubator system (Live Cell Instrument). A 488-nm diode laser (Cobolt) was used to visualize the beta-actin mRNA and the fluorescence emission was filtered with a 525/50 band-pass filter (Chroma). To observe F-actin in live neurons, a 561-nm diode laser (Cobolt) was used and the fluorescence emission was filtered with 630/75 band-pass filter (Chroma). Due to photobleaching, the temporal scale of mRNA imaging was different according to the purpose of experiment. For comparing the movement of mRNA in dendrite and axon, ~1 min long time-lapse image was taken at 5~20 frames per second (fps). For the mRNA imaging moving in the axonal sub-compartment, the time-lapse images were acquired in 1~0.2 fps for 1~15 min. For the dual color imaging of F-actin and β-actin mRNA, the time-lapse images were acquired in 0.2 fps for 1~20 min.

5.2.4 Single-molecule fluorescence *in situ* hybridization (smFISH)

Hippocampal neuron cultures at DIV 11 were transfected with CMV-GFP-UtrCH by using lipofectamine 2000 (Thermo Fisher). The next day, neurons were fixed by 4% paraformaldehyde followed by 10 min washing with phosphate-buffered saline (PBS) supplemented with 1mM MgCl2 (PBSM). To permeabilize the neurons, neurons were then treated in 0.1% Triton X-100 in PBS for 10 min. After twice washing in PBSM, cultures were preincubated for 10 min in prehybridization buffer containing 50% formamide, 2×SSC in RNase-free water and were hybridized overnight at 37˚C in hybridization buffer containing 2× SSC, 10% formamide, 10% dextran sulfate, bovine serum albumin (20 mg/ml), sheared salmon sperm DNA, *E. coli* tRNA and 50 mer DNA probes. We designed three kinds of Quasar 570 dye (Biosearch) conjugated probes, (i) LK20 (5’-TTT CTA GAG TCG ACC TGC AG-3’), (ii)

LK51-1 (5'-CTA GGC AAT TAG GTA CCT TAG-3') and (iii) LK-51-2 (5'-CTA ATG AAC CCG GGA ATA CTG-3'), to target the MBS linker sequence. The neurons were then washed with the prehybridization buffer, followed by washing with 2×SSC and PBSM. smFISH images were acquired on an Olympus IX73 inverted wide-field microscope by using U Apochromat 150× 1.45 NA TIRF objective (Olympus). Two-channel 16×16 grid z-stack (from -10 μm to 10 μm every 0.4 μm) imaging was performed for a large view of axon branches. The 488-nm diode laser (Cobolt) and 561-nm diode laser (Cobolt) were used for visualization of F-actin and β-actin mRNA, respectively. The fluorescence emissions were filtered by 525/50 and 630/75 band-pass filters and simultaneously detected by two EMCCD cameras. To analyze the β-actin mRNA in axons, we first stitched the grid images and segmented the axons using custom written MATLAB scripts. To detect the mRNA FISH particles, we used FISH-quant software. We then classified the mRNA particle manually whether the mRNA was colocalized with actin patches or not.

5.2.5 Data analysis

To analyze the mRNA movement, we cropped the region with mRNA and straightened using Fiji software. We then classified each mRNA according to its subcellular locations (boutons, filopodia and shaft). The mRNA signal in the axon is too dim to track automatically, we used a tracking program, HybTrack [*14*], which combined manual and automatic tracking. To assess the mobility of mRNA particle, the mean squared displacement,ρ_n, was calculated from N-frame-long mRNA track by using the following formula

$$\rho_n = \rho(n\Delta t) = \sum_{i=1}^{N-n} ((x_{i+n} - x_i)^2 + (y_{i+n} - y_i)^2)/(N-n)$$

where Δt is the frame interval, x_i and y_i are the coordinates of the mRNA particle at i^{th} frame. The exponent of MSD, β, is calculated by linear fitting from log-scaled MSD. The fitting range was different depending on the length and interval of the mRNA track (For 5~20 fps image ~1 min long: 1~2 sec; for 0.2~1 fps image 1~15 min long: 3~9 sec; for 0.2 fps image 1~20 min long: 10~40 sec). mRNA tracks taken at 5~20 fps were used to calculate the diffusion coefficient, which was obtained by (the slope of MSD from 200 ms to 400 ms)/4.

To measure the speed of the mRNA, we measured the run length and run time of the section where the mRNA moves more than 1.5 μm in one direction (anterograde or retrograde).

5.3 Results and Discussion

5.3.1 Imaging fluorescently labeled β-actin mRNA in live axons

The MCPxMBS mouse not only expresses green fluorescence protein (GFP) fused MS2 bacteriophage capsid protein (MCP-GFP), but also 24 repeats of MS2 binding site (MBS) was inserted into the 3' untranslated region of the β-actin gene (Fig. 5.1A). The MBS RNA stem-loop has a specific binding to MCP, allowing the β-actin mRNA to be labeled with up to 48 GFP molecules. To separate axons from other cellular compartments of neurons, we cultured the hippocampal neurons of the postnatal (P1) mouse on the one side of a microfluidic device in which 500 μm long narrow channels are place in the middle (Fig. 5.1B) [*15*]. The channels act as a 'filter' to isolate axons from cell bodies and dendrites. The axon randomly grew through channels and we could observe the endogenous axonal β-actin mRNA on the other side of the cultured region using highly inclined and laminated optical sheet (HILO) microscopy. We could obtain the tracks of β-actin mRNAs by using HybTrack software in which a tracking software combines manual and automatic detection [*14*].

5.3.2 Comparison of axonal and dendritic β-actin mRNA movement

We found a qualitative difference in movements of β-actin mRNAs in axon and dendrite (Fig. 5.1C). Unlike β-actin mRNAs in dendrite that showed rest and run motion phase, the majority of axonal β-actin mRNAs exhibited confined diffusive movement. To characterize the movement of mRNA, we calculated the mean squared displacement (MSD) of mRNA tracks (Fig. 5.1D). The MSD of diffusing molecule can be written as $\sim\tau^{\beta}$ and the type of diffusion can be classified according to the value of β ($0 < \beta < 1$: subdiffusion, $\beta > 1$: superdiffusion) which can be obtained by linear fitting in log-log scale [*16, 17*]. We found dendritic mRNAs had higher β value than axonal mRNAs (Fig. 5.1F), which indicates dendritic mRNAs moves more freely than axonal mRNAs. However, the axonal mRNAs showed higher diffusion coefficient than dendritic mRNAs (Fig. 5.1G). Moreover, by measuring the speed of mRNA from the part of track where the mRNA moved more than 1.5 um in one direction, we found the dendritic mRNA had a higher speed than the axonal mRNA (Fig. 5.1H). Taken together, the axonal mRNAs were less mobile and slower than dendritic mRNAs, but more diffusive, which suggest the mRNA localization in axons and dendrites is facilitated by different localization mechanisms.

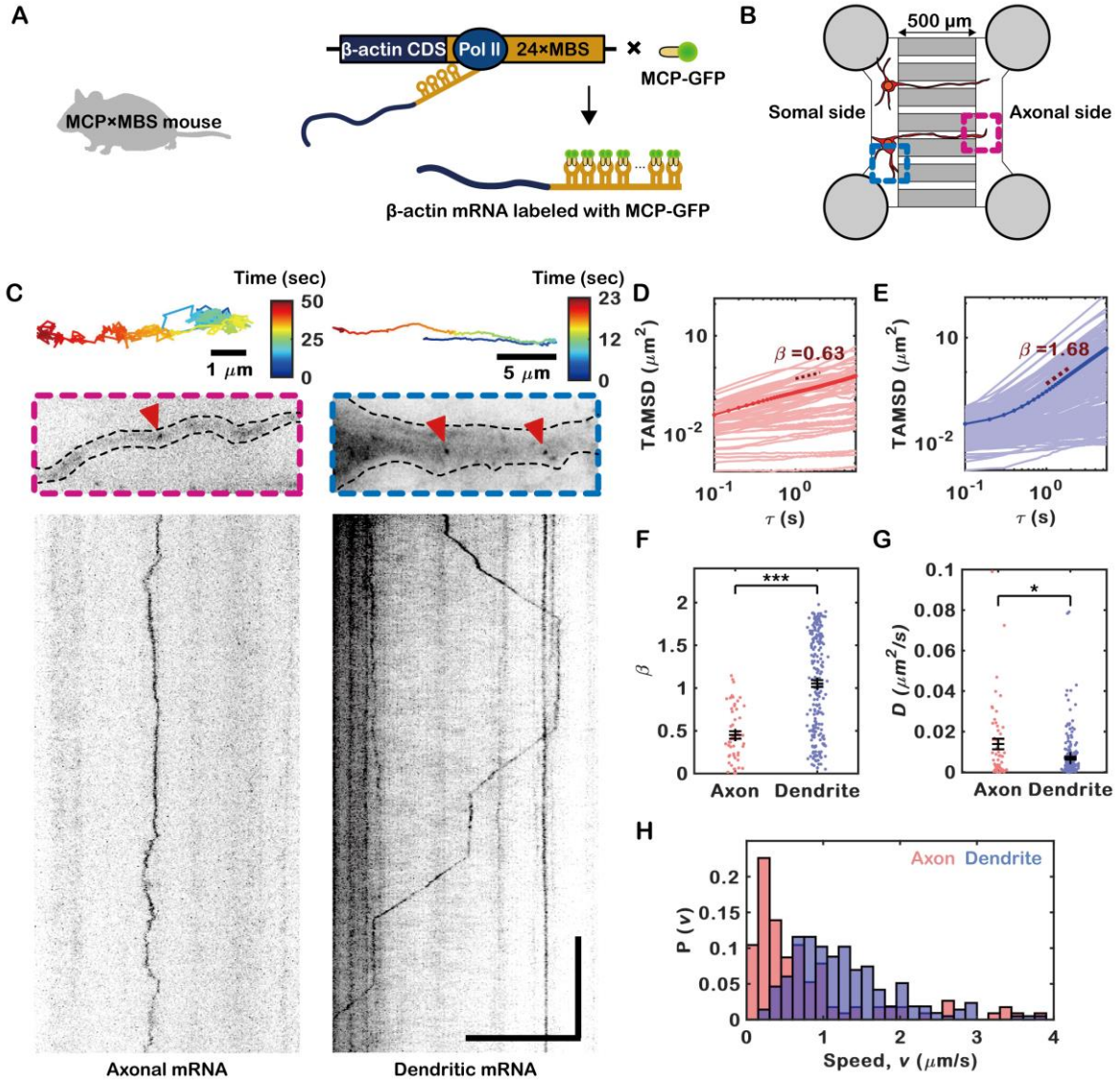

Fig. 5.1. Comparison of movement dynamics of axonal and dendritic mRNA. (A) Schematic for labeling the β-actin mRNA. MS2 bacteriophage capsid protein (MCP) binds to MS2 binding site (MBS) RNA stem-loop with a high specificity and affinity. By crossing the MBS knock-in mouse and MCP-GFP mouse, a transgenic mouse which expresses endogenous β-actin mRNA labeled with GFP can be generated. **(B)** Schematic diagram of the PDMS device consisted of four reservoirs and dozens of 500 μm long channels. Neurons were cultured in one side of the chamber and axons grew along the channels. **(C)** Top, example tracks of axonal and

dendritic mRNA colored by time. Middle, Representative snapshot of time-lapse image of mRNA in axon (left) and dendrite (right). Red arrows indicate the β-actin mRNAs. Bottom, kymographs of time-lapse images. The horizontal and vertical axis represents position and time, respectively. Scale bars: (horizontal) 10 μm and (vertical) 10 sec. **(D-E)** The mean squared displacement (MSD) of axonal (D, n = 53 mRNAs) and dendritic (E, n = 215 mRNAs) mRNA tracks. The thick lines indicate the average of MSD values. **(F)** The MSD exponent of axonal and dendritic mRNA (*** $P < 10^{-10}$ by two-sample Kolmogorov - Smirnov test). **(G)** The diffusion coefficient of axonal and dendritic mRNA (* $P < 0.05$ by two-sample Kolmogorov - Smirnov test). **(H)** The probability distribution of speed of axonal (red) and dendritic mRNAs (blue).

Motion types of axonal mRNA in bouton, filopodia and axon shaft.

We next examined if there are preferential mRNA motion types according to the location of mRNA. We investigate the mRNA tracks based on the location of mRNA; bouton, filopodia and shaft (Fig. 5.2A). We found some mRNA localized in the boutons or near filopodia showing subdiffusive motion (Fig. 5.2A, left and middle). Occasionally, we observed the traveling mRNAs in the shaft change the motion type near a potential filopodia (Fig. 5.2A, right panel). The filopodium elongated a few minutes after the mRNA localization (Fig. 5.3). We first calculated the MSD of the mRNA in each subcompartment (Fig. 5.2B). We found the mRNA in axon shafts showed more mobile movement than in other subcompartments (Fig. 5.2C). To identify the transient motion types, we used HMM-bayes software [*18*]. Though most of the mRNA showed diffusive or stationary motion, 7.7 % of mRNAs in the shaft showed directed motion (Fig. 5. 2D). Collectively, the data indicate that mRNAs travel in the shaft and dock at the bouton or filopodia for the potential local translation.

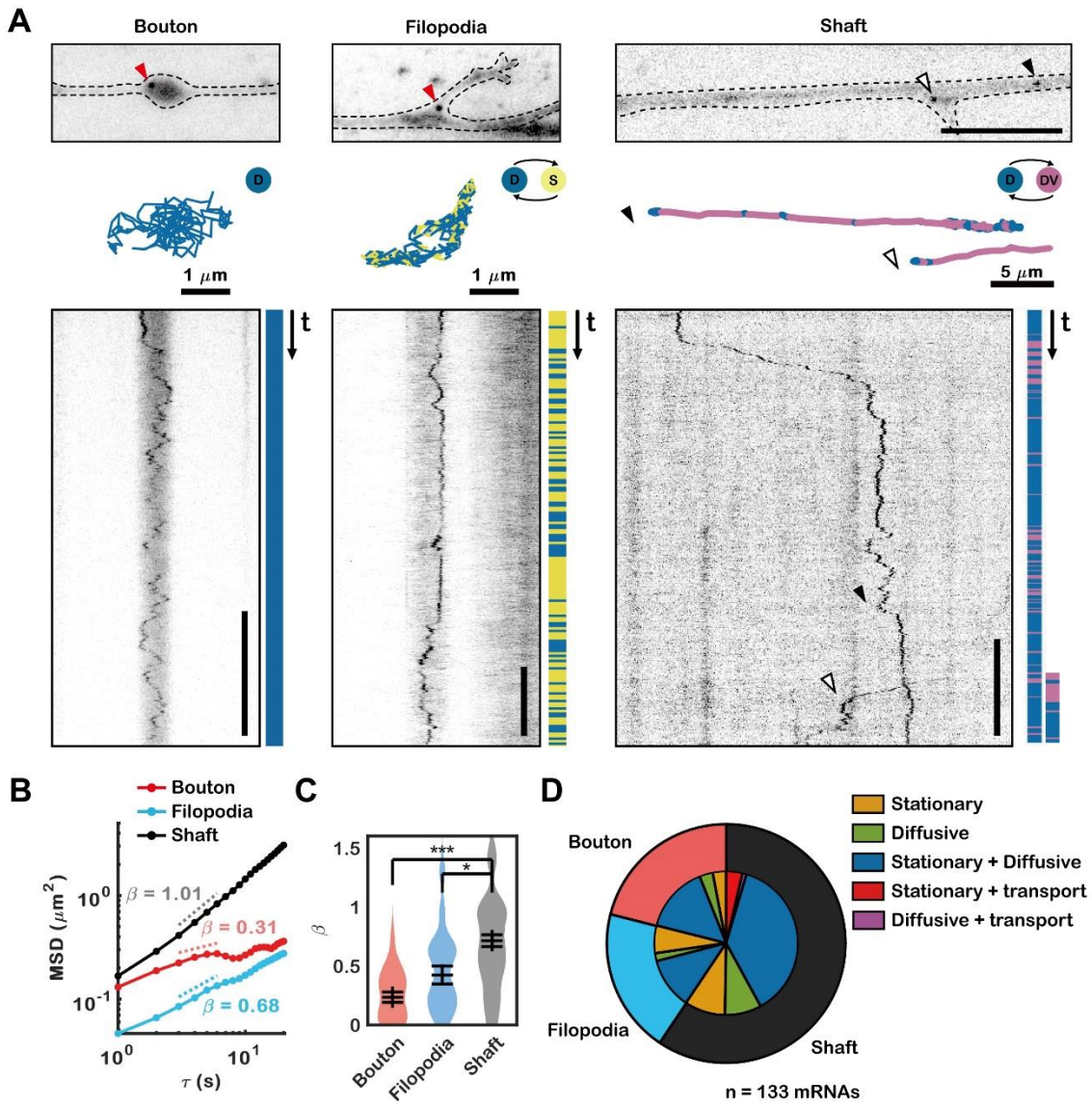

Fig. 5.2. Localization and dynamics of the axonal β-actin mRNA in bouton, filopodia, and shaft. (A) Example images of axonal β-actin mRNA in bouton (left), filopodia (middle) and shaft (right). The movement of mRNA was characterized by HMM-bayes. D, diffusive; S, stationary; DV, directed transport. Scale bars: (Horizontal) 10 µm, (vertical, left and middle) 10 sec, (vertical, right) 5 min. (B) The average of MSD of tracks of mRNA in bouton, filopodia, and shaft. (C) The MSD exponent value of mRNAs in bouton, filopodia, and shaft (*** $P < 10^{-4}$, * $P < 0.05$ by two-sample Kolmogorov - Smirnov test). (D) A pie plot representing the proportion of mRNA localized in different sub-compartments and their fraction of motions

types.

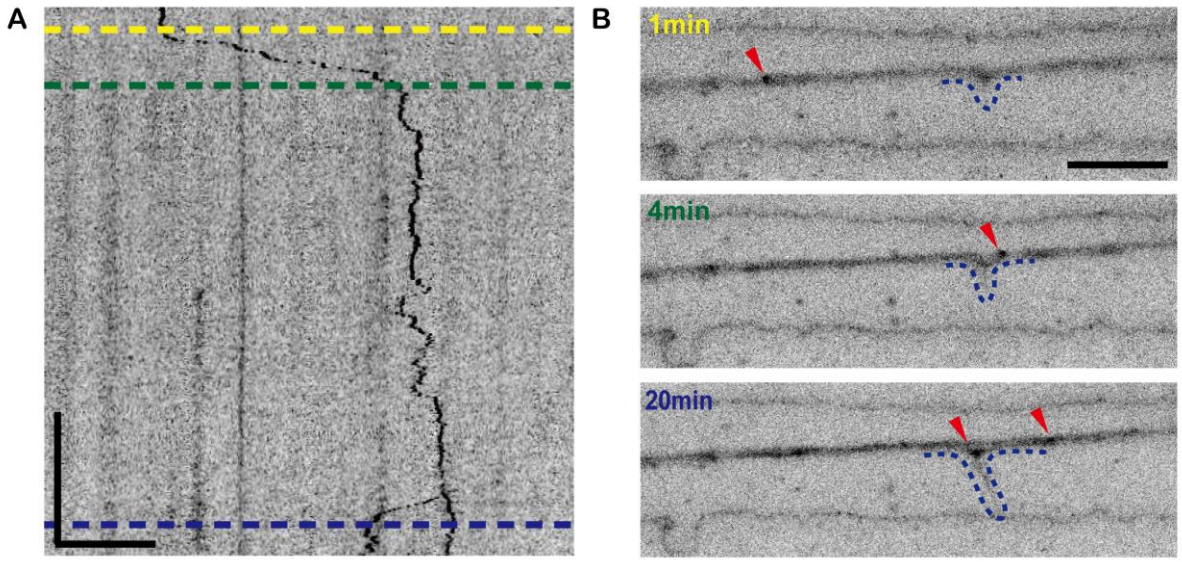

Fig. 5.3. (A) A kymograph of a time-lapse image of the right panel of Fig. 2A. **(B)** Images of three time points (1 min, 4 min and 20 min in yellow, green and blue dotted line in (A), respectively). Two mRNAs were localized nearby a potential filopodium, and a filopodium developed after a few minutes.

5.3.3 Colocalization of β-actin mRNA with actin patches

Although some mRNA showed transport motion in the shaft, most of the mRNA showed stationary or diffusive motion. The β-actin mRNA has a cis-acting element that interacts with Zipcode binding protein (ZBP1) in which one of RNA binding protein (RBP) is known to be associated with an actin-based motor protein, MyosinVa [*19*]. Moreover, in dendrites, the localization of β-actin mRNA to dendritic spine has been reported to require the F-actin network [*8*]. Since filopodia and boutons were known to be the actin-rich areas [*20*], we hypothesized the β-actin mRNA localization in axons is facilitated by F-actin patches. To see

the colocalization of β-actin mRNA and APs, we transfected neurons with GFP fused the calponin homology domain of utrophin (GFP-UtrCH) which allows to visualize F-actin and performed single-molecule fluorescence in situ hybridization (smFISH) targeting MBS linker sequence on the following day (Fig. 5.4A). The transfection sparsely expressed GFP-UtrCH (~20 neurons per dish) which allows to identify the axon of the neuron by morphology. To observe the β-actin mRNA in axons at a wide scale, we performed grid imaging with a high magnified microscope followed by 3D segmentation and particle detection (Fig. 5.4B). Along the axons, we could find APs where the F-actin signal was distinctly bright (Fig. 5.4C). We found 70 ± 5.1 % of mRNAs were colocalized with APs (Fig. 5.4D).

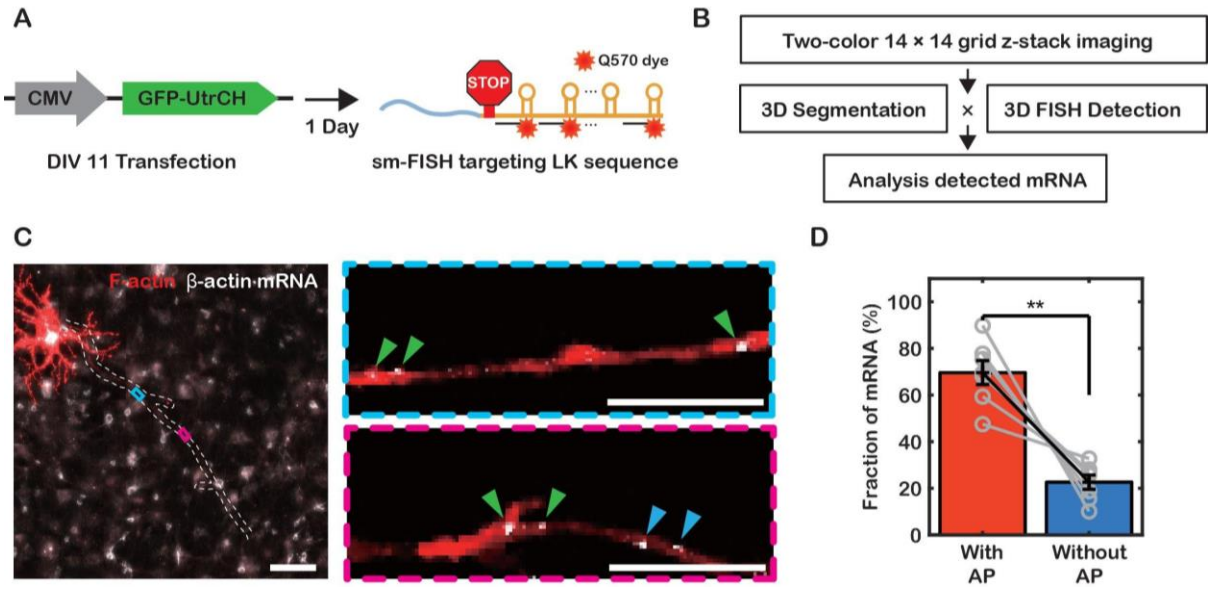

Fig. 5.4. smFISH targeting β-actin mRNA on the sparsely transfected neurons. (A) On DIV 11, neurons were transfected with CMV-GFP-UtrCH for labeling F-actin and smFISH was performed smFISH on the following day. **(B)** To image widely spread axons, grid imaging was performed followed by a stitching process. Using 3D segmentation of axons and 3D particle detection, β-actin mRNAs in axon were identified. **(C)** Left, a representative image of

smFISH image. The wide dotted line indicates the axon. Right, enlarged images of the blue and pink box in the left panel. Green arrows indicate the mRNA within actin-patches and blue arrows indicate the mRNAs outside of the actin patch. **(D)** The fraction of β-actin mRNA categorized by their location and colocalization with actin patches (n = 7 axons, 367 mRNAs).

5.3.4 The movement of β-actin mRNA within actin patches

We next examined the relation between the motion type of β-actin mRNA and APs. To observe the AP and β-actin mRNA simultaneously, we sparsely transfected the MCP×MBS mouse neurons with mCherry-UtrCH and performed simultaneous imaging of F-actin and β-actin mRNA with a HILO microscope equipped with two cameras. The axonal β-actin mRNAs were often observed to be trapped in the AP (Fig. 5.5A, left). Occasionally, we could observe some motile mRNAs were stochastically anchored into the AP (Fig. 5.5A, right). Using HMM-bayes approach, we inferred the transient motion type of mRNA and classified the motion type into stationary, diffusive and transport. When the mRNA switched the motion type from transport state to diffusive or stationary state, we referred to the event as “docking”. The mRNA showed docking at the point where the F-actin signal was higher than the median value of F-actin signal in axons (Fig. 5.5B). We then segmented APs by thresholding F-actin images, and analyzed the β-actin mRNA tracks with and without APs. The mRNA tracks without APs showed larger MSD than the mRNA tracks with APs (Fig. 5.5C). When the mRNAs were colocalized with APs, the β value of MSD was lower (Fig. 5.5D) which indicates the mRNA are less mobile in the APs. Moreover, the mRNAs were more likely to show transport state when mRNAs were not colocalized with APs (Fig. 5.5D). We also observed a β-actin mRNA passing through an AP, and after the passage, a small fragment of F-actin was moving together (Fig. 5.6). This observation suggests the axonal β-actin RNP directly interacts with actin patches (Fig. 5.6C). Together, our results show that β-actin mRNA travels through the axon shaft and stochastically

docking at the APs for potential branch formation.

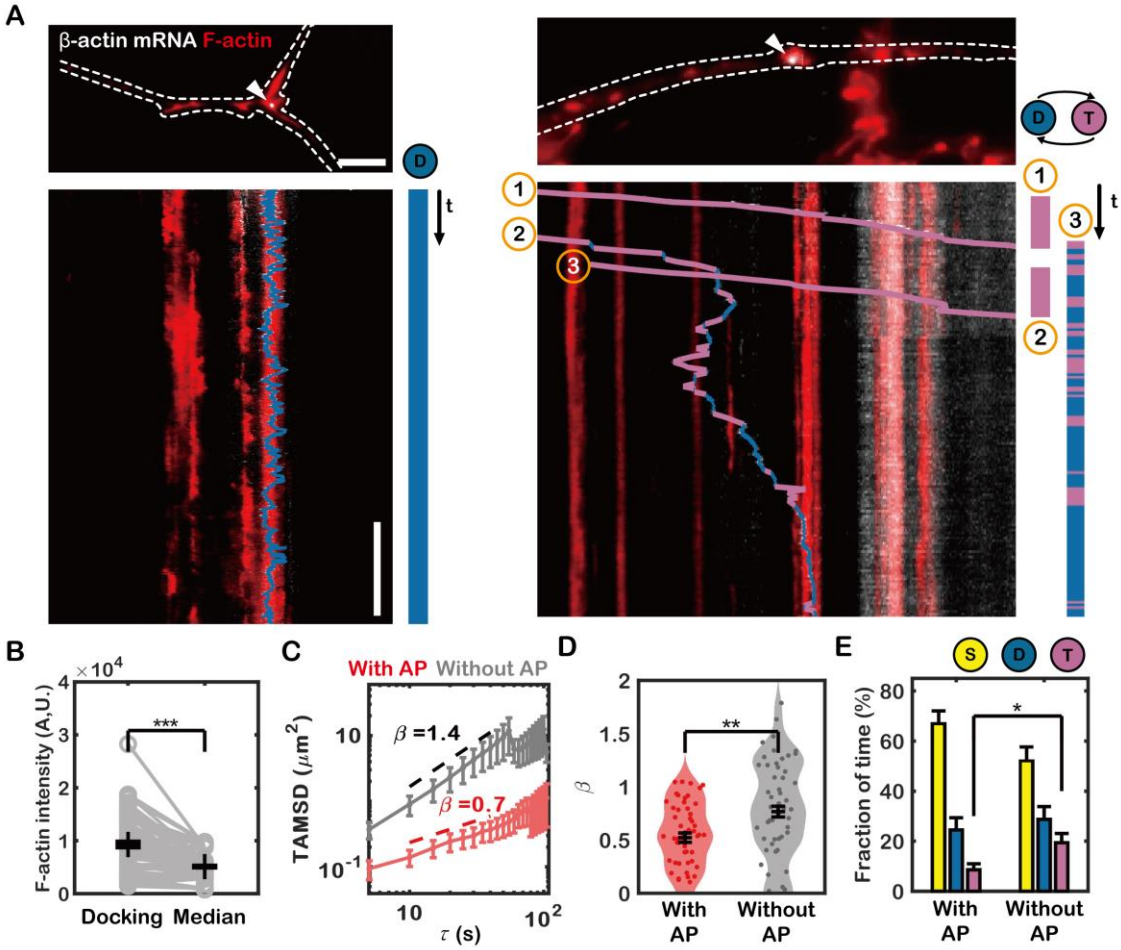

Fig. 5.5. Dual-color imaging of F-actin and mRNA in live neurons. (A) Left, example image of an axonal mRNA localized in an actin patch and a kymograph of the time-lapse image. HMM-bayes classified the movement of the mRNA as a diffusive motion. Right, three mRNAs passing through an axon. The first and third mRNA showed purely transport motion without docking. However, the second mRNA showed mixed movement of diffusive and transport and docked into the actin patch. (B) The F-actin intensity at the docking site of mRNA was higher than the median value of F-actin intensity of axon (n = 78 mRNAs, *** $P < 10^{-12}$ by pairwise *t* test). (C) The MSD of tracks of mRNA inside (red) and outside (gray) of actin patches. (D) The distribution of MSD slope value, β, calculated from the tracks of mRNA with AP and

without AP (** $P < 0.01$ by two-sample Kolmogorov- Smirnov test). (E) The proportion time that mRNA moved in motion type of stationary, diffusive, and transport (* $P < 0.05$ by two-sample Kolmogorov - Smirnov test).

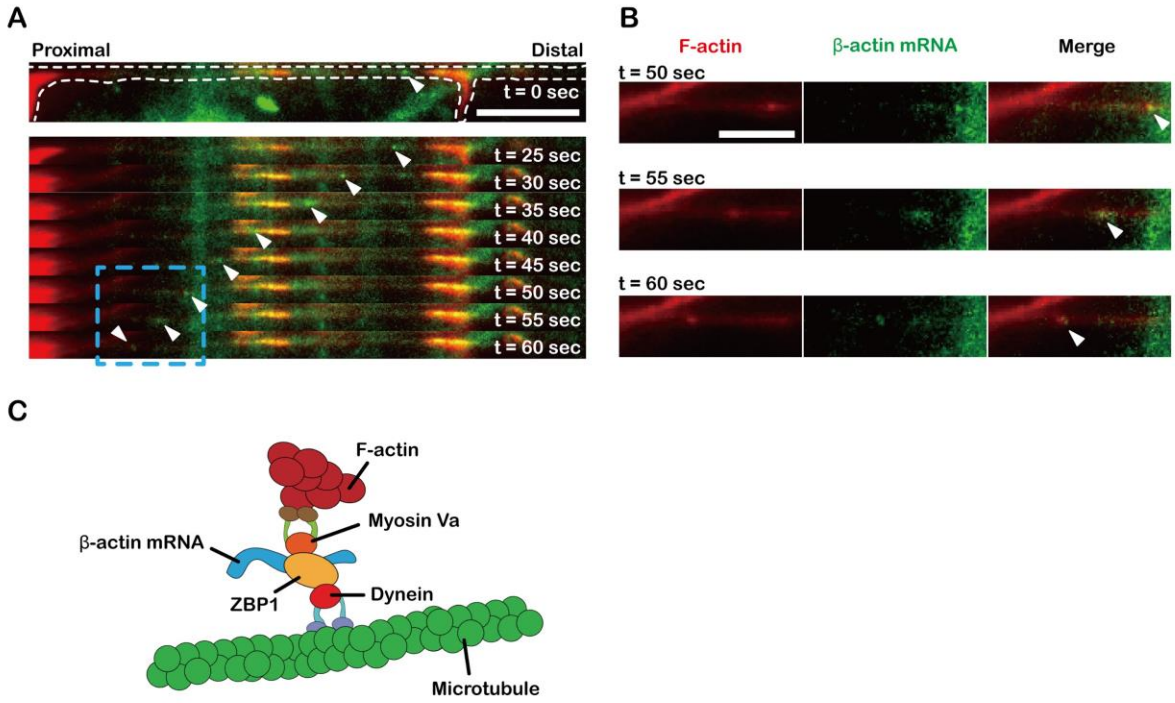

Fig. 5.6. (A) Dual color time-lapse images of β-actin mRNA and F-actin. A β-actin mRNA was retrogradely transported and passed through an actin patch. After passing through the actin patch, the β-actin mRNA was transported with a F-actin fragment. **(B)** Enlarged images of the blue dotted box in (A). (C) A hypothetical scheme of the mRNA in (B). The mRNP particle including ZBP1, β-actin mRNA, MyosinVa and Dynein is transported on the microtubule by carrying a fragment of F-actin. Scale bars, (A) 10 μm and (B) 5 μm.

5.3.5 Discussion

The single-molecule imaging of endogenous β-actin mRNA has allowed us to observe the

localization process in real time. Previous studies have provided valuable information about the β-actin mRNA localization and translation in axons using nonspecific labeling of RNA and UTRs conjugated fluorescence reporters [*9, 21*]. However, these methods have limitations in that they cannot observe the localization process of a specific mRNA species. Our approach of the MS2 system for the visualization of β-actin mRNA showed how the motion type of β-actin mRNA is different in dendrites and axons. Though the movement of β-actin mRNA is generally sub-diffusive motion in axons, some mRNAs showed super-diffusive transport in the axon shaft. The smFISH experiment showed that the β-actin mRNA is localized in the F-actin rich area. By imaging F-actin and β-actin mRNA simultaneously in live axons, we found that the β-actin mRNA docks to the actin patch which is a precursor of axonal filopodia or branches [*22*].

Our results show a different motion type according to the location of β-actin mRNA in the axonal subcompartment. A previous study on β-actin mRNA trafficking in axons using molecular beacon also reported that the β-actin mRNA movement was different in the axon shaft and growth cone [*7*]. Moreover, the study demonstrated the anchoring of β-actin mRNA by the actin filament in the growth cone, as has been observed in fibroblast. This result is in line with our observation of β-actin mRNA docking at the actin patches. In addition, ZBP1, the RNA binding protein of β-actin mRNA, is associated with actin-based motor protein MyosinVa [*19*]. The knock down of Myosin increases the number of motile ZBP1 particles. We found that a β-actin mRNA is transported retrogradely with a F-actin fragment, suggesting the β-actin mRNA interacts directly with actin patch by MyosinVa. Collectively, the axonal β-actin mRNPs associated with ZBP1 and MyosinVa are transported along the axon shaft and localized into the actin filament rich regions.

Our observation shows that mRNAs anchor rather than make actin patches. The actin patch is

known to be formed by the PI3K pathway along the axons, and known as a precursor of branch formation [*22*]. The translational machinery including rRNA, mRNAs, mitochondria exists at the branch points [*9*]. Previous work has shown that emergence of new branches requires de novo local β-actin synthesis [*21*]. Therefore, the role of β-actin mRNA localized at actin patches is to provide the β-actin protein for potential filopodia/branch formation.

5.4 References

1. C. E. Holt, K. C. Martin, E. M. Schuman, Local translation in neurons: visualization and function. *Nat Struct Mol Biol* **26**, 557-566 (2019).
2. H. S. Jung, B. C. Yoon, C. E. Holt, Axonal mRNA localization and local protein synthesis in nervous system assembly, maintenance and repair (vol 13, pg 308, 2012). *Nat Rev Neurosci* **13**, (2012).
3. B. Turner-Bridger, C. Caterino, J. M. Cioni, Molecular mechanisms behind mRNA localization in axons. *Open Biol* **10**, (2020).
4. C. Eliscovich, A. R. Buxbaum, Z. B. Katz, R. H. Singer, mRNA on the Move: The Road to Its Biological Destiny. *J Biol Chem* **288**, 20361-20368 (2013).
5. A. R. Buxbaum, G. Haimovich, R. H. Singer, In the right place at the right time: visualizing and understanding mRNA localization (vol 16, pg 95, 2015). *Nat Rev Mol Cell Bio* **16**, 513-513 (2015).
6. M. A. Kiebler, G. J. Bassell, Neuronal RNA granules: Movers and makers. *Neuron* **51**, 685-690 (2006).
7. B. Turner-Bridger *et al.*, Single-molecule analysis of endogenous beta-actin mRNA trafficking reveals a mechanism for compartmentalized mRNA localization in axons. *P Natl Acad Sci USA* **115**, E9697-E9706 (2018).
8. Y. J. Yoon *et al.*, Glutamate-induced RNA localization and translation in neurons. *P Natl Acad Sci USA* **113**, E6877-E6886 (2016).
9. M. Spillane, A. Ketschek, T. T. Merianda, J. L. Twiss, G. Gallo, Mitochondria Coordinate Sites of Axon Branching through Localized Intra-axonal Protein Synthesis. *Cell Rep* **5**, 1564-1575 (2013).
10. M. S. Song, H. C. Moon, J. H. Jeon, H. Y. Park, Neuronal messenger ribonucleoprotein transport follows an aging Levy walk. *Nature Communications* **9**, (2018).
11. H. C. Moon, H. Y. Park, Imaging Single mRNA Dynamics in Live Neurons and Brains. *Method Enzymol* **572**, 51-64 (2016).
12. K. M. Leung *et al.*, Cue-Polarized Transport of beta-actinm RNA Depends on 3 ' UTR and Microtubules in Live Growth Cones. *Front Cell Neurosci* **12**, (2018).
13. H. Y. Park *et al.*, Visualization of Dynamics of Single Endogenous mRNA Labeled in Live Mouse. *Science* **343**, 422-424 (2014).
14. B. H. Lee, H. Y. Park, HybTrack: A hybrid single particle tracking software using manual and automatic detection of dim signals. *Sci Rep-Uk* **8**, (2018).

15. A. M. Taylor *et al.*, A microfluidic culture platform for CNS axonal injury, regeneration and transport. *Nat Methods* **2**, 599-605 (2005).
16. R. Metzler, J. H. Jeon, A. G. Cherstvy, E. Barkai, Anomalous diffusion models and their properties: non-stationarity, non-ergodicity, and ageing at the centenary of single particle tracking. *Phys Chem Chem Phys* **16**, 24128-24164 (2014).
17. I. Golding, E. C. Cox, Physical nature of bacterial cytoplasm. *Phys Rev Lett* **96**, (2006).
18. N. Monnier *et al.*, Inferring transient particle transport dynamics in live cells. *Nat Methods* **12**, 838-+ (2015).
19. V. C. Nalavadi *et al.*, Regulation of Zipcode Binding Protein 1 Transport Dynamics in Axons by Myosin Va. *J Neurosci* **32**, 15133-15141 (2012).
20. C. Dillon, Y. Goda, The actin cytoskeleton: Integrating form and function at the synapse. *Annu Rev Neurosci* **28**, 25-55 (2005).
21. H. H. W. Wong *et al.*, RNA Docking and Local Translation Regulate Site-Specific Axon Remodeling In Vivo. *Neuron* **95**, 852-+ (2017).
22. A. Ketschek, G. Gallo, Nerve Growth Factor Induces Axonal Filopodia through Localized Microdomains of Phosphoinositide 3-Kinase Activity That Drive the Formation of Cytoskeletal Precursors to Filopodia. *J Neurosci* **30**, 12185-12197 (2010).

6. Conclusion and outlook

This study can be divided to two part. The first part, Arc mRNA transcription imaging in live mice, I first demonstrated the visualization of Arc mRNA transcription in live animal using transgenic knock-in PCP×PBS mice in which all neuronal Arc mRNA is labeled with up to 48 GFPs. In the second part, the visualization of β-actin mRNA transport in live axons, I studied how the axonal β-actin mRNA can be transported in the live axons.

In Chapter II, I observed the Arc mRNA transcription using two-photon excitation microscope. In about 30% of neurons, the Arc transcription sites were emerged after the contextual fear conditioning. Using smFISH, I confirmed that the locus signal in the nucleus is the Arc mRNA transcription site and found ~15 mRNAs are in the transcription site. Moreover, with our observation of transcription site signal reaches at 6 min after the stimulation and decay to half in 2.5 min, we generated a simulation to compare with conventional methods. The simulation result showed that our methods has higher temporal accuracy and less sensitive to the intensity threshold and basal activity. For the first time, this study observed the Arc mRNA transcription site in live animal and demonstrated the PCP×PBS mouse for the identification of Arc+ neurons.

In Chapter III, questioning what pattern of neuronal ensemble activated during memory encoding and retrieval, I performed mapping of Arc+ neurons in CA1 and RSC across multiple days. After CFC, the mice repeatedly retrieved the fear memory for 3 days. I found the CA1 neurons relatively less re-activated upon memory retrieval than RSC neurons. Interestingly, in CA1, the re-activation rate was similar during memory retrieval and exposure to new environment (context B). However, the reactivation rate of RSC was significantly higher during retrievals in which ~4% of neurons consistently reactivated

during encoding and three retrievals. Moreover, the re-activation rate was correlated with the freezing rate which indicates the reactivation rate in RSC reflects the degree of memory recall. To further investigate the memory retrievals in remote times, I mapped Arc+ neurons in CA1 and RSC for one month. Similar with recent memory, CA1 neurons rapidly turnover, whereas 4% of RSC neurons constantly activated during encoding and all retrieval sessions. Within the idea of hippocampal indexing theory, our result can be interpreted that the CA1 neuronal ensembles are allocated not only to the memory encoding but also to each retrieval and the RSC ensembles are consistently contains the information about the memory. Considering the fact that RSC is a direct downstream region of CA1, the result that 4% of neuronal ensemble in RSC consistently express Arc suggests the possibility of a pattern completion mechanism despite dynamic CA1 input. The idea of pattern completion mechanism between hippocampus and neocortex was also predicted in the hippocampal indexing theory.

In Chapter IV, to answer the role of re-expressing ensemble and others, I performed the calcium imaging with Arc transcription mapping with virtual reality experiment. The Arc+ neurons showed higher neural activity than Arc- neurons, as expected. Implementing encoding, recall, and new encoding paradigm using VR, I investigate the relation of neural activities and Arc expression patterns. Interestingly, the neurons expressed Arc both during encoding and recall showed high theta frequency tuned (6-10 Hz) activity during encoding and recall, but not in new environment. Unexpectedly, these neurons are not coupled themselves, whereas place cells formed dense cluster. These results suggest the Arc re-expressing neurons convey the memory information through theta-burst.

This study demonstrated the new way to study the gene expression in live animals. There are two key advantages in our approach. First, the direct and real-time observation of transcription has high temporal accuracy on resolving the gene expression event. The IEG-promotor driven reporter expression has at least 2 hours of lag time, which makes difficult

to deconvolution of gene expression event. This advantage allows to map Arc+ neurons in the same region repeatedly for 1 month. Second, our method can be combined with other kinds of measurement such as calcium imaging. Using virtual reality system, I found the subset of neuronal population has memory specific bursting activity during the memory encoding and recall. This data first observed the role of consistently Arc expressing neurons and compared with the neurons that doesn't re-expressing Arc.

Though this study provided the Arc expressing pattern during memory tests, several questions are remained. First, to confirm that the Arc re-expressing neurons are the essential part for the memory representations, loss/gain of function studies are required using optogenetic or chemogenetic activation. To artificially activate the subset of neurons, the recently developed holographic activation or light-induced Cre activation approach can be used. This future study will give the information of casual relation between gene expression and memory storage. Second, to investigate the neural activity of Arc expressing neurons in neocortex, the same experiment can be performed imaging in the neocortex such as RSC or prefrontal cortex. Lastly, with the benefit of real-time imaging of IEG expression and calcium imaging, our method can be used to reconcile the attractor model and engram field.

In the second part of the dissertation (Chapter V), to investigate the mRNA localization in axons, I observed the β-actin mRNA in live axons using MCP×MBS mouse in which β-actin mRNAs are fluorescently labeled with up to 48 GFPs. Culturing neurons in microfluidic devices, I could separate axons from dendrites and somas. Unlike dendritic mRNA which showed clear moving and rest motion, axonal mRNAs showed sub-diffusive motion. When the mRNA localized at axonal shaft, the mRNA often showed directed transport motion and localized to axonal filopodia or boutons. By dual-color imaging of β-actin mRNA and F-actin, I found the sub-diffusive β-actin mRNA were trapped in the F-actin hotspot, so-called 'actin patch'. This study firstly showed that β-actin mRNA localized to the actin patch in the

axons, which suggests potential branch formations through translation of β-actin mRNA. Collectively, using the advantage of visualization of mRNA in live cells or animals, this thesis demonstrated this technique can be used to identify the memory-related neuronal ensemble, and to study the localization of mRNA in neurons. This *in vivo* RNA imaging approach has potential to unravel the dynamics of neuronal population underlying various learning and memory processes.

Abstract in Korean (국문초록)

살아있는 뉴런과 동물에서 mRNA 관찰에 대한 연구

서울대학교 물리천문학부
물리학 전공
이병훈

mRNA는 유전자 발현의 첫번째 산물이면서, 리보솜과 함께 단백질을 합성한다. 특히 뉴런에서, 몇몇 RNA들은 자극에 의해 만들어지고, 뉴런의 특정 부분으로 수송되어 국소적으로 단백질 양을 조절할 수 있게 한다. 최근 mRNA 표지 기술의 발전으로 살아있는 세포에서 단일 mRNA를 관찰하는 것이 가능해졌다. 이 연구에서, 우리는 RNA 이미징 기술을 이용해, 기억 형성과 상기할 때 활성화된 뉴런의 집합을 찾는 것 뿐 아니라, 뉴런의 축삭돌기에서 mRNA가 어떻게 수송되는지를 관찰했다.

이 논문의 첫 부분에서 우리는 신경 자극에 반응해서 만들어지는 것으로 알려진, Arc 유전자의 전사를 관찰하였다. 기억은 engram 혹은 기억 흔적 (memory trace)라고 불리는 뉴런들의 집합에 저장되어 있다고 생각된다. 그러나, 시간에 따라서 이런 기억 흔적세포들의 집합이 어떻게 변하고, 변화하면서도 어떻게 정보를 유지할 수 있는지 잘 알려져 있지 않다. 또한, 살아있는 동물에서, 기억 흔적세포를 긴 시간 동안 여러 번 찾아내는 것은 어려운 일이었다. 이 연구에서는 genetically-encoded RNA indicator (GERI) 기술을 사용해, 기억 흔적세포의 표식으로 널리 사용되는 Arc mRNA의 전사과정을 살아있는 쥐에서 관찰하였다. GERI를 이용함으로써, 기존 방법들의 한계점이었던 시간 제약 없이, 실시간으로 Arc를 발현하는 뉴런들을 찾아낼 수 있었다. 쥐에게 공간 공포 기억을 주고

나서 여러 번 기억을 상기시키는 행동실험 후에 Arc를 발현하는 세포를 식별했을 때, CA1에서는 Arc를 발현하는 세포가 이틀 후에는 더 이상 활성화되지 않았으나, RSC의 경우 4퍼센트의 뉴런들이 계속해서 활성화하는 것을 관찰했다. 신경활동과 유전자 발현을 같이 조사하기 위해, 쥐가 가상 환경을 탐험하고 있을 때 GERI와 칼슘 이미징을 동시에 진행하였다. 그 결과, 기억을 형성할 때와 상기시킬 때 Arc를 발현했던 뉴런들이 기억을 표상하는 것을 알아낼 수 있었다. 이처럼 GERI 기술을 이용해 살아있는 동물에서 유전자 발현된 세포를 찾아내는 방식은 다양한 학습 및 기억 과정에서 기억 흔적세포의 dynamics에 대해 알아낼 수 있을 것으로 기대된다.

이 논문의 두번째 부분에서, 우리는 세포 골격의 기본 구성 단위가 되는 β-actin의 mRNA를 축삭돌기에서 관찰하였다. mRNA의 국소화 (localization)를 통한 국소 단백질 합성은 축삭돌기 (axon)의 성장과 재생에 중요한 역할이 있다고 알려져 있다. 하지만, 아직 mRNA의 국소화가 축삭돌기에서 어떻게 조절되고 있는지 잘 알려져 있지 않다. 이 문제를 해결하기 위해서, 우리는 모든 β-actin mRNA가 형광으로 표지된 유전자 변형 쥐를 이용해, 살아있는 축삭돌기에서 β-actin mRNA를 관찰하였다. 이 쥐의 뉴런을 축삭을 구분해 줄 수 있는 미세유체 장치 (microfluidic device)에 배양한 뒤에, β-actin mRNA를 관찰하고 추적을 진행했다. 축삭은 세포 몸통으로부터 길게 자라기 때문에 mRNA가 먼 거리를 수송되어야 함에도 불구하고, 대부분의 mRNA가 수상돌기에 비해 덜 움직이고 작은 영역에서 움직이는 것을 보았다. 우리는 β-actin mRNA가 주로 축삭돌기의 가지가 될 수 있는 filopodia 근처와, 시냅스가 만들어지는 bouton 근처에 국소화되는 것을 관찰했다. Filopodia와 bouton이 actin이 풍부한 부분으로 알려져 있기 때문에, 우리는 액틴 필라멘트와 β-actin mRNA의 움직임간에 연관성을 조사했다. 흥미롭게도, 우리는 β-actin mRNA가 액틴 필라멘트와 같이 국소화 되고, β-actin mRNA가 액틴 필라멘트 안에서 sub-

diffusive한 움직임을 보였으며, 먼 거리를 움직이던 mRNA도 액틴 필라멘트에 고정되는 모습도 확인할 수 있었다. 축삭에서 β-actin mRNA 움직임을 본 이번 관찰은 mRNA 수송 및 국소화에 대한 생물물리학 적 메커니즘의 기반이 될 수 있을 것이다.

핵심어: Arc mRNA, 전사, 이광자 현미경, 가상 현실, 신경 활동 이미징, 기억의 형성과정, 살아있는 동물에서의 촬영, β-actin mRNA, 축삭 돌기, 액틴 패치, 미세유체 장치

학번: 2015-20344